universität wien

MASTERARBEIT / MASTER'S THESIS

Titel der Masterarbeit / Title of the Master's Thesis

Atomic and molecular beam methods for matter wave interferometry

verfasst von / submitted by

Linus Noah Ian Fynn Kulman BSc

angestrebter akademischer Grad / in partial fulfilment of the requirements for the degree of

Master of Science (MSc)

Wien, 2025 / Vienna, 2025

Studienkennzahl lt. Studienblatt / degree programme code as it appears on the student record sheet:	UA 066 876
Studienrichtung lt. Studienblatt / degree programme as it appears on the student record sheet:	Masterstudium Physics
Betreut von / Supervisor:	Univ.-Prof. Dr. Markus Arndt

Abstract

Matter-wave interferometry has become a key tool for exploring the quantum-classical transition and for precision measurements of fundamental constants, inertial forces, and molecular properties. Extending these techniques to polypeptides and proteins in molecular beams under high vacuum opens the possibility to study molecular complexity and probe quantum effects at increasingly macroscopic scales. However, biomolecular interferometry is particularly challenging due to the complexity of these compounds, which often precludes ionization. Accordingly, new strategies are required to manipulate and detect neutral molecules at the low kinetic energies characteristic of matter-wave experiments.

This thesis discusses the generation of coherent beams, optical beam-splitting strategies for molecules that cannot be easily ionized, and the detection of neutral massive particles with superconducting nanowire detectors. These detectors exploit the sensitivity of the superconducting state to thermal excitations. We demonstrate that it is possible to detect metastable atoms and neutral molecules with kinetic energies of only a few electronvolts, at efficiencies exceeding those of conventional secondary electron multipliers by more than six orders of magnitude. In addition, photocleavage experiments with ruthenium complexes are presented as a model for studying molecular fragmentation processes. We demonstrate additionally the diffraction of metastable Helium, which may later serve in the alignment stage of a future matter-wave interferometer.

Zusammenfassung

Interferometrie mit Materiewellen hat sich zu einem zentralen Werkzeug entwickelt, um den Übergang zwischen Quanten- und klassischer Physik zu untersuchen und Fundamentalkonstanten, Inertialkräfte und molekulare Eigenschaften mit hoher Präzision zu messen. Die Ausdehnung dieser Verfahren auf Polypeptide und Proteine in Molekularstrahlen unter Hochvakuumbedingungen eröffnet die Möglichkeit, molekulare Komplexität zu erforschen und Quanteneffekte auf zunehmend makroskopischen Skalen sichtbar zu machen. Da viele Biomoleküle aufgrund ihrer Komplexität nicht ohne Weiteres ionisiert werden können, sind neue Strategien erforderlich, um sie im neutralen Zustand und bei den für Materiewellenexperimente typischen niedrigen kinetischen Energien als Strahlen zu präparieren und nachzuweisen.

Diese Arbeit behandelt die Erzeugung kohärenter Strahlen, optische Strahlteilerstrategien für schwer ionisierbare Moleküle sowie die Detektion neutraler Moleküle mit supraleitenden Nanodrahtdetektoren. Die Funktionsweise der Detektoren beruht auf der hohen Empfindlichkeit des supraleitenden Zustands gegenüber thermischen Anregungen. Wir demonstrieren den Nachweis metastabiler Atome und neutraler Moleküle mit kinetischen Energien von nur wenigen Elektronenvolt bei Wirkungsgraden, die jene herkömmlicher Sekundärelektronenvervielfacher um mehr als sechs Größenordnungen übertreffen. Als Modellsystem für molekulare Fragmentationsprozesse werden Photospaltungsexperimente mit Rutheniumkomplexen vorgestellt. Zudem demonstrieren wir die Beugung metastabilen Heliums, das künftig in der Justage eines Interferometers für Biomoleküle eingesetzt werden könnte.

Contents

1. Introduction

1.1. Matter-waves

In 1923, Louis de Broglie postulated that any isolated portion of matter or energy could be associated with a periodic phenomenon [1]. In the same year, Arthur Compton published his findings showing that photons transfer momentum during scattering events, unequivocally demonstrating the wave-particle duality of light [2]. While light had long been understood as a wave and only later shown to exhibit particle-like properties, de Broglie's proposal took the reverse approach by attributing wave-like behavior to matter. The de Broglie wavelength λ_{dB} of this phenomenon is[1]:

$$\lambda_{\mathrm{dB}} = \frac{h}{p} \,. \tag{1.1}$$

The matter-wave depends solely on the particle's (relativistic) momentum p and the Planck constant h as a proportionality factor. De Broglie proposed that this wave would be of "very great importance in determining the motion of any moving body" and that an atom's path through multiple slits would be diffracted analogously to light waves [1]. This inspired Schrödinger to search for a differential equation to describe this non-classical behavior, ultimately leading him to develop his equation for wavefunction propagation [4] which laid the groundwork for more advanced field-theoretic formulations, including the Dirac equation [5].

1.1.1. Milestones in matter-wave diffraction

Experimental validation of matter-waves came in 1927, just four years after de Broglie's proposal, when Davisson and Germer successfully diffracted electrons using a nickel crystal [6]. In 1930 Estermann and Stern diffracted helium atoms and dihydrogen (H_2), thereby extending the range of viable diffraction candidates to molecules [7]. Neutron diffraction was conducted independently by Mitchell [8] and by Halban and Preiswerk [9], but it only gained broader recognition after Wollan used it to investigate crystallographic structures in 1945 [10].

Milestones in the following decades were primarily achieved in atom interferometry, where diffraction at optical [11, 12] and mechanical gratings [13] was demonstrated. In the early 1990s, both Ramsey-Bordé [14, 15] and Kasevich-Chu [16] interferometers employed spectroscopic

[1] De Broglie originally defined the phase wave frequency of the associated periodic phenomenon as $\nu_{\mathrm{dB}} = \gamma m_0 c^2/h$, where $\gamma = 1/\sqrt{1-\beta^2}$ is the Lorentz factor, and m_0 is the particle's rest mass. The corresponding phase velocity is $v_{\mathrm{ph}} = c/\beta$. Using the relation $\lambda\nu = v_{\mathrm{ph}}$, it follows that $\lambda_{\mathrm{dB}} = hc/(\gamma m_0 \beta c^2) = h/(\gamma m_0 \beta c) = h/p$, with the relativistic momentum given by $p = \gamma m_0 \beta c$. This relation also holds for particles with rest mass $m_0 = 0$, where $p = E/c$ [3].

techniques to establish superpositions between atom paths, resulting in interference. The realization of Bose-Einstein condensation also confirmed the role of the thermal de Broglie wavelength in governing atomic interactions and determining the critical temperature for the onset of macroscopic ground-state occupation [17, 18].

Molecule interferometry

Interference with molecules larger than dimers remained a challenge for several decades after Estermann and Stern's first experiment. To observe interference between two waves, reliable beam splitting methods are needed. Spectroscopic techniques such as Ramsey-Bordé interferometry have been successfully applied to iodine (I_2) interference [19]. However, due to the high internal complexity of large molecules, methods relying on entanglement between internal and external states or on efficient cycling transitions are not applicable. This was overcome when in 1999 interference of C_{60} molecules at a silicon nitride grating, based solely on their center-of-mass momentum was successfully demonstrated [20]. Importantly, the experiment showed that macroscopic ensembles share a common de Broglie wavelength and diffract as a whole, independent of their internal molecular states. Since then, the size and mass of molecules that could be shown to interfere have been pushed to macroscopic scales, with the current record reaching over 2,000 atoms and molecular masses up to $m = 25\,\mathrm{kDa}$ per compound [21].

1.2. Motivation and overview

1.2.1. Diffraction of biomolecules

An intriguing aspect of the interferometry of complex molecules is the diffraction of biomolecules. Diffraction of large molecules and clusters makes it possible to probe the boundaries between quantum and classical, everyday physics. Beyond that, the diffraction and delocalization of biomolecules, such as vitamins and peptides, the building blocks of life, raise even deeper questions about the quantumness of nature. Apart from this rather philosophical motivation, experiments with matter-waves can be used to extract a wide range of information about atoms and molecules. In typical setups, de Broglie wavelengths are smaller than atomic radii, making even small phase shifts readily detectable [22]. Interferometric force sensing has been employed to assess the electrical, optical, and dynamical properties of vitamins and peptides. Because these experiments are conducted with atomic and molecular beams in the gas phase, they enable the study of such molecules and their internal complexity in an idealized environment, free from perturbations caused by solvents or different environmental conditions [23, 24]. Such quantum metrology techniques are of particular interest for large neutral biomolecules, whose analytical study has remained challenging due to their fragility [22].

1.2.2. Thesis outline

This thesis addresses the three essential components for biomolecular diffraction: sources, coherent beam splitters, and detectors. Each aspect is discussed theoretically and complemented by experimental demonstrations in the respective chapters.

Chapter 2 describes the generation and manipulation of molecular beams, focusing on supersonic expansion, beam preparation, and mass spectrometry. *Chapter 3* introduces the principles of diffraction and interference, including a demonstration of diffraction with metastable helium. Mach–Zehnder-style interferometers with metastable helium could be employed as stable and well-characterized reference systems to calibrate and align future protein interferometers, providing a reliable benchmark before operating with larger and more fragile biomolecules. The mechanisms underlying photon-absorption-based optical beam splitters are then examined in *Chapter 4*. Future implementations of coherent beam splitters for biomolecules will likely rely on ionization and recoil following photocleavage [25]. We demonstrate efficient cleavage of a compound as an example for such mechanisms. Finally, matter-wave interference with slow neutral beams requires correspondingly efficient detectors. *Chapter 5* presents recent progress on superconducting nanowire detectors, which have us enabled to detect metastable atoms and neutral molecules with kinetic energies as low as 3.45 eV [26].

While interferometry with biomolecules such as insulin remains a challenge, the methods presented here aim to extend matter-wave experiments into this regime. Progress in this direction tests the persistence of quantum coherence in increasingly complex systems and opens possibilities for quantum-enhanced sensing and structural studies of biomolecules in the gas phase [27, 28].

2. Atomic and molecular beams

Producing molecular beams with sufficient brightness, velocity control, and coherence is essential for matter-wave diffraction. Depending on the application, different source properties are required. For neutral detection with superconducting nanowires, tunable velocities and narrow spreads enable precise time-of-flight measurements, while in diffraction experiments the beam velocity sets the de Broglie wavelengthλ_{dB} and must be well defined to maintain coherence. Extending such studies to larger molecules further demands slow beams with long coherence lengths, while minimizing collisional decoherence.

This chapter focuses on the Even–Lavie valve, the supersonic source used for both the diffraction experiments in Chapter 4 and the production of metastable atoms and neutral molecules in Chapter 5. It outlines the principles of supersonic beam generation, skimming, and valve operation, including its dielectric barrier discharge module for metastable atom production. In addition, we describe the ion-beam methods required for photocleavage studies in Chapter 4, where electrospray ionization (ESI) transfers intact ruthenium complexes into the gas phase, followed by quadrupole and time-of-flight mass selection.

2.1. Supersonic beams and the Even–Lavie valve

Supersonic expansion beams have allowed for progress in various fields, one prominent of them being matter-wave interferometry [29]. They provide intense, cold, and directed atomic beams with velocity spreads of $\sim 10\%$. Such low spreads enhance the resolution of diffration patterns, which enabled the first demonstrations of atom diffraction at nanomechanical gratings [13]. In the experiments presented here, an Even–Lavie (EL) valve is used to generate a pulsed beam of metastable helium. The following section introduces the essential principles of supersonic expansion, beam collimation, and metastable production, focusing on their relevance for diffraction experiments.

2.1.1. Supersonic expansion

In a supersonic source, gas at stagnation pressure p_0 and temperature T_0 is released into vacuum through a nozzle. Collisions in the early expansion convert internal energy into forward motion, resulting in strong internal cooling of the transverse degrees of freedom and a sharp forward velocity distribution [30, 31, 32]. The beam thus acquires high brightness and a narrow angular spread, both essential for producing transverse coherence, which we will discuss in 3.3.

The expansion can be approximated as adiabatic and isentropic in the near-field behind the nozzle, where it forms the characteristic Mach disk enclosed by barrel shocks [31]. Inside the disk, an anisotropic partition of the thermal energies in the beam greatly reduces the thermal motion both perpendicular and parallel to the beam flow direction in favor of the forward velocity [32]. This is important for matter-wave applications, because a reduction of the whole velocity spread around the beam's mean velocity increases the coherence downstream, for reasons we discuss in 3.3. The eventual terminal velocity v_{terminal} of a particle with mass m and adiabatic index γ follows from energy conservation:

$$v_{\text{terminal}} = \sqrt{3\gamma \, \frac{k_{\text{B}} T_0}{m}} \, . \tag{2.1}$$

For a monoatomic gas ($\gamma = 5/3$) this reduces to $v_{\text{terminal}} = \sqrt{5 k_{\text{B}} T_0 / m}$, in good agreement with experimental data for noble gases [33]. Helium, as the second-lightest atom and the lightest noble gas, provides the fastest beams and is therefore commonly used as a carrier gas in supersonic expansions with different molecules [34, 33].

2.1.2. Skimming the beam

Without skimming, the supersonic expansion continues until it is disrupted by the normal shock at the Mach disk. Its position is governed by the nozzle diameter d and the ratio of the source backing pressure to the chamber pressure. In the experiments we present here, this ratio was on the order of 10^9, corresponding to a Mach disk distance of about $10^4 d$ [31], which is one meter for our 100 µm nozzle. To isolate the cold beam before these shock structures, the central part of the expansion is extracted by a skimmer, which preserves the low divergence of the supersonic core [35]. When choosing the nozzle–skimmer distance, it should be noted that at approximately one tenth of the Mach disk length, collisions in the expansion have typically frozen out and the beam reaches continuous flow [31, 36]. The exact skimmer geometry is optimized to minimize interactions between the transmitted beam, the reflected plume, and the skimmer walls. At sufficiently high densities, such reflections can generate additional shock waves in the supersonic regime. These lead to heating and introduce entropy into the flow, effectively "clogging" the beam and degrading its thermal properties [29]. Clogging partly depends on the pressure ratio between source and chamber [33, 29]. Accordingly, in our experiments, we chose source pressures to maximize brightness while avoiding clogging effects. In practice, the skimmer also serves as the differential pumping aperture, enabling operation at high stagnation pressure in the source chamber while maintaining low background pressure in the experimental region. Figure2.1 shows a schematic of skimming in supersonic expansion.

2.1.3. The Even–Lavie valve

The Even–Lavie (EL) valve is a pulsed supersonic source widely adopted in molecular and atom optics [33]. Compared to continuous sources, pulsed sources combine high brightness with reduced gas load. Gas is only released in short pulses, allowing much higher backing pressures while maintaining low average background pressure at the same vacuum pumping power [31].

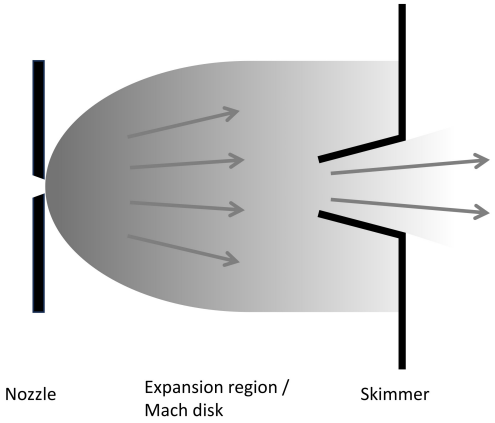

Figure 2.1.: Supersonic expansion and skimming. Gas at expands through a nozzle into vacuum, forming a Mach disk. A skimmer extracts the cold, low-divergence core before shock-induced reheating of the beam. Adapted from [31].

When employing the EL valve, the source chamber pressure should be kept below1×10^{-5} mbar to ensure free expansion. Typically, this can already be achieved with turbomolecular pumps of $\approx 500\,\mathrm{L\,s^{-1}}$, which is less than one tenth of the pumping power required for continuous sources [33, 37]. This makes the source particularly suitable for diffraction experiments, where high particle flux and long coherence times are required. The valve has even been employed in biomolecular diffraction experiments, where noble gas pulses entrain laser-desorbed molecules into coherent beams suitable for interferometry [22]. It is also possible to directly seed molecules into a noble gas expansion, where they evaporate via vapor pressure and are picked up and accelerated by the carrier gas. Experiments have shown that biomolecules can be internally cooled to temperatures below $T < 1\,\mathrm{K}$ in helium expansions [34].

Mechanically, the valve employs a magnetic actuator driving a spring-loaded plunger to open and close a trumpet-shaped nozzle. It operates at repetition rates between 1 and 550 Hz and achieves minimum pulse widths of 10 µs [33], which ranks it among the fastest electromagnetically actuated pulsed sources [36]. The nozzle geometry optimizes cooling in the early expansion and results in brighter beams than pinhole designs. A single pulse of duration $\simeq 20\,\mu\mathrm{s}$ releases on the order of 10^{15} atoms, with a velocity spread of about 10% [37, 33]. The valve can be operated over a wide range of stagnation temperatures (4–550 K) without mechanical adjustment, providing considerable experimental versatility [33]. Temperature control is particularly important for seeded gases, as it allows the gas load to be tuned according to the proximity to the vaporant's vapor pressure [38].

2.1.4. Dielectric barrier discharge metastable source

To generate metastable atoms, the Even–Lavie valve can be equipped with a dielectric barrier discharge (DBD) mounted directly at the nozzle exit [37, 33]. The DBD consists of concentric

electrodes separated by a thin dielectric and is driven by nanosecond-scale high-frequency pulses. This configuration produces a spatially uniform discharge while suppressing arc formation, allowing efficient excitation without significant heating of the beam [37, 39]. As a result, about 10^{-4} to 10^{-3} of the atoms in the beam are excited into metastable states [37].

For helium, this yields atoms in the 2^3S_1 state ($E = 19.82\,\text{eV}$ above the ground state, $\tau \approx 7870\,\text{s}$) [40], which decay via a weak magnetic-dipole transition in the extreme ultraviolet [41]. For argon, the $^3P_2$ metastable state is produced ($E = 11.55\,\text{eV}$ above the ground state, $\tau \approx 55\,\text{s}$) [40]. Figure2.2 shows the energy level diagrams of these transitions.

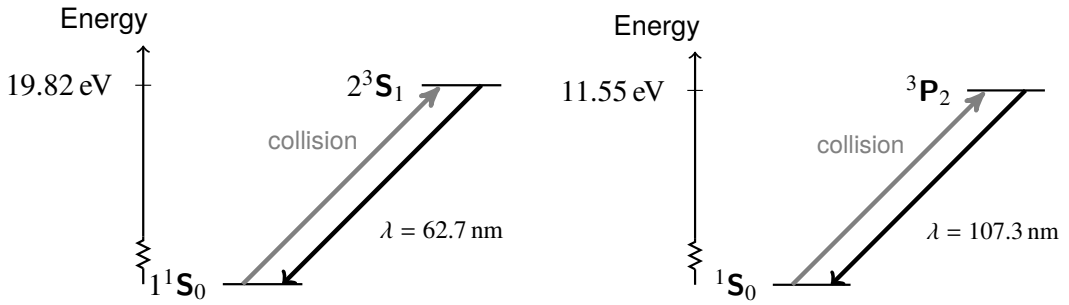

(a) Helium (b) Argon

Figure 2.2.: Energy level diagrams of metastable triplet states excited by the dielectric barrier discharge of the Even–Lavie valve in (a) helium and (b) argon.

In chapter 3, we discuss the diffraction of metastable helium. Its long lifetime, high internal energy, and electrical neutrality make it particularly well suited for nanomechanical diffraction studies. Metastable argon, on the other hand, plays an important role in the characterization of the superconducting detectors discussed in chapter 5.

2.2. Ionization methods

Experimenting with beams of neutral biomolecules is challenging, as their motion is unaffected by electromagnetic fields. Many sources require initial ionization of the molecules to transfer them into the gas phase, where they can then be neutralized, cooled, or otherwise prepared. Here, we present two ionization methods that are used throughout the thesis. Electrospray ionization (ESI) as the primary method for generating beams of ruthenium complexes, and electron impact ionization (EI) in combination with quadrupole mass spectrometry as a diagnostic tool to characterize residual background gases in the detector chamber.

2.2.1. Electron impact ionization

Electron impact ionization (EI) operates by colliding neutral molecules with high-energy electrons, causing electron ejection and ion formation. Acceleration voltages are usually 60−100 eV, while

the electron current ranges from 50 to 400 µA, depending on the size and operating temperature of the filament. Ions generated by EI are predominantly singly charged. Higher electron energies, while enhancing ionization efficiency, also increase the likelihood of fragmentation and generally coincide with a wider variety of ion species [42]. The physics behind fragmentation is discussed in more detail in chapter 4.

For more fragile compounds like biomolecules, soft ionization techniques like matrix-assisted laser desorption/ionization (MALDI) [43, 44], or electrospray ionization are able to achieve ionization without fragmentation.

2.2.2. Electrospray ionization

Electrospray ionization (ESI) is a soft ionization technique that transfers intact molecular ions from solution into the gas phase. A solution containing the analyte is fed through a capillary held at a high potential relative to a counter-electrode. The actual ionization already occurs in the solution, where the charge sign of the ions depends on whether protonation or deprotonation processes dominate. For this reason, ESI works especially well for polar molecules, such as biomolecules. After reaching the gas phase, ions are then brought into vacuum via differential pumping stages. The resulting electric field forms a Taylor cone at the capillary tip, from which a fine jet of charged droplets is emitted. Through repeated evaporation and fission, these droplets shrink until single analyte molecules remain, now in the gas phase as multiply charged ions [42]. The process is sketched in figure 2.3.

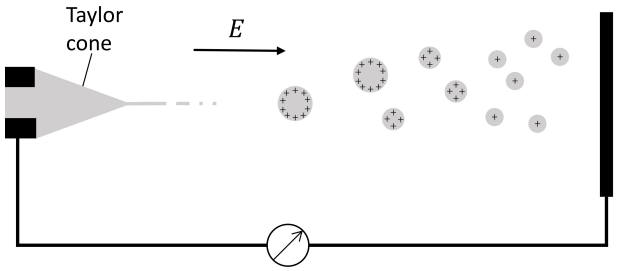

Figure 2.3.: Schematic of electrospray ionization (ESI) operating in positive mode. A high electric field at the capillary tip forms a Taylor cone and emits a charged microjet that breaks into droplets. Evaporating droplets reach the Rayleigh limit and fission, yielding multiply charged gas-phase ions. Adapted from [42].

This method is markedly soft and well-suited for fragile biomolecules and complex molecules [45]. Its ability to transfer intact macromolecules into the gas phase without fragmentation has made ESI central to biological mass spectrometry, where it enabled the analysis of proteins and other large species, earning it the reputation of providing "wings for molecular elephants" [46]. Molecular charge states corresponding to masses up to 80 kDa/e have been reported with ESI [47].

Droplet formation and disintegration

At the capillary tip, the strong electric field deforms the liquid into a Taylor cone, from which a jet of charged droplets emerges [48, 42]. As solvent evaporates, charge density increases until the Rayleigh limit is reached, where electrostatic repulsion overcomes surface tension. While this process is often described as a sudden "Coulomb explosion," experiments show that droplets instead elongate and emit smaller, highly charged progeny droplets [49]. These secondary droplets then become themselves unstable, leading to a cascade of evaporations and fissions until only nanodroplets containing single analyte molecules remain. Complete desolvation then produces gas-phase ions, typically in multiple charge states. If lower charge states are required, post-ionization charge reduction can be applied [45].

2.2.3. Ion beam transport and selection

Once ions are transferred into the gas phase, they move through a transfer capillary into a vacuum, typically with pressures of a few millibar. The capillary acts as a skimming device for the ions and as differential pumping stage. Transfer optics, both direct current (DC) ion funnels and radiofrequency (RF) multipoles guide the ions to the mass spectrometer. In multipoles, alternating voltages are applied to sets of rods which generates an effective confining potential in the radial direction. Ions that travel along the multipole axis are radially trapped by the oscillating fields [42].

In 4.4, a quadrupole mass filter is employed along with a hexapole guide. Quadrupoles posses well-defined stability regions, that allow only ions within a narrow m/z range to be transmitted, thus enabling species selection [50]. Higher-order multipoles such as hexapoles lack sharply defined stability boundaries but offer larger acceptance and transmit a broader m/z range with high efficiency, making them well suited for transport [51].

After ions are transferred into the gas phase, they enter a capillary that guides them into the vacuum region at pressures of a few millibar. The capillary acts as a skimming device for the ions and as differential pumping stage. From there, the beam is guided by electrostatic funnels and radiofrequency (RF) multipoles, where alternating voltages perturb the ion trajectories. Depending on the applied fields and frequencies, only ions within certain m/z ranges remain confined near the axis on average, enabling efficient transmission. Ions outside this stable range are removed from the beam, so that multipoles already act as pre-filters for subsequent analysis [42].

In 4.4, a quadrupole mass filter is employed along with a hexapole guide. Quadrupoles possess well-defined stability regions that allow only ions within a narrow m/z range to be transmitted, thus enabling species selection [50]. Higher-order multipoles such as hexapoles lack such sharply defined stability boundaries but offer larger acceptance and transmit a broader m/z range with high efficiency, making them well suited for transport [51].

2.3. Mass spectrometry

Mass spectrometry (MS) separates and identifies ions according to their mass-to-charge ratio m/z. A typical setup consists of an ion source, a mass analyzer, and a detector [42]. Different techniques are characterized by their ionization technique and the type of analyzer employed. We discuss here the two types of mass spectrometers used in the experimental work of this thesis. A time-of-flight (TOF) analyzer was employed to study the photocleavage of ruthenium complexes (section 4.4), and a quadrupole mass spectrometer was used to monitor residual gases and fragments in the SSPD experiments (section 5.3). The following subsections summarize the principles of operation of each.

2.3.1. Time-of-flight mass spectrometry

In a time-of-flight (TOF) analyzer, ions are separated by their different velocities after acceleration in an electric field. when an ion with charge $q = ez$ is accelerated through a voltage U is acquires the kinetic energy Uq, corresponding to a velocity change Δv of:

$$\Delta v = \sqrt{\frac{2Uq}{m}} \propto \sqrt{\frac{z}{m}} \,. \tag{2.2}$$

The travel time over a distance s is therefore:

$$t = \frac{s}{v} \propto s\sqrt{\frac{m}{z}} \,, \tag{2.3}$$

so that the arrival time at the detector provides a direct measure of the mass-to-charge ratio [42].

In the system used in 4.4, an orthogonal acceleration scheme is combined with an electrostatic reflector. Orthogonal acceleration decouples the longitudinal beam velocity from the pulsed acceleration used for mass analysis, which minimizes the impact of the initial velocity spread. The reflector compensates for small energy differences by forcing faster ions onto longer trajectories, further adding to their separation and thereby improving mass resolution [52, 42].

2.3.2. Quadrupole mass spectrometry

Quadrupole mass analyzers transmit ions of a specific mass-to-charge ratio (m/z) by confining their trajectories in combined RF and DC electric fields applied to four parallel rods. Opposite rods are held at equal potential, with neighboring rods at opposite polarity. The resulting quadrupole potential confines ions in the transverse plane, where their motion is governed by the Mathieu equations [53]. These describe the oscillatory motion in the x and y directions in terms of the dimensionless parameters a and q. For a quadrupole with distance r_0 from the center to the rods, static bias voltage U, and RF component V at frequency ω_0, the parameters for an ion of mass m_i

are:

$$a_x = -a_y = \frac{4ezU}{m_i r_0^2 \omega_0^2} \propto U \,,$$
$$q_x = -q_y = \frac{2ezV}{m_i r_0^2 \omega_0^2} \propto V \,. \tag{2.4}$$

Each m/z value has distinct ranges of U and V where the corresponding Mathieu parameters are stable, such that the ions remain on axis and reach the detector. This stability region takes on a "tongue"-shaped form, where the apex corresponds to a unique m/z value at a fixed U/V ratio. By ramping both voltages simultaneously while keeping their ratio constant, different masses can be scanned sequentially. Varying the U/V ratio shifts the operating point within the stability region, as higher ratios give sharper mass selection but lower transmission, while lower ratios broaden the transmitted range and increase sensitivity at the cost of resolution [51, 42]. This operating principle is visualized in the stability diagram in figure 2.4, where only ions with Mathieu parameters inside the gray tongue-shaped region are transmitted through the quadrupole. Even under real conditions, the transmission ranges exhibit sharply defined boundaries, making quadrupoles highly effective as mass filters [51].

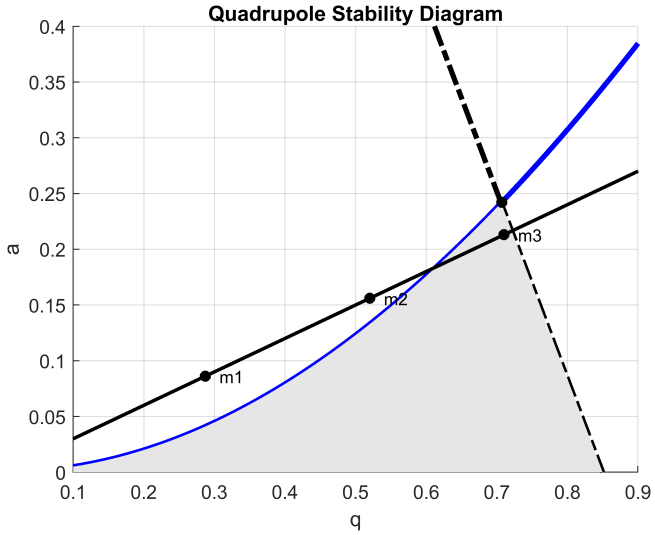

Figure 2.4.: Stability diagram of a quadrupole mass filter in Mathieu parameter space. Only ions with parameters falling into the grey region remain stable in both transverse directions and are transmitted, while all others are filtered out. By scanning RF and DC voltages at a fixed ratio $U/V \propto a/q$, corresponding to the solid black line in the diagram, different m/z values can be selected. Adapted from [53].

3. Diffraction & interference

Diffraction is a fundamental wave phenomenon. According to Huygens' principle, every point on a wavefront acts as the source of a secondary spherical wave, and the observed wavefront is the envelope of these elementary contributions [54]. Because spherical waves radiate in all directions, they can propagate into the geometric shadow of an obstacle. At an edge, for instance, the envelope wavefront bends into the shadowed region. This mechanism enables the transport of intensity, such as light or a quantum mechanical wave function, into areas inaccessible by purely geometric or classical trajectories.

Interference arises when multiple coherent waves are superimposed. Their amplitudes add linearly, and the resulting intensity is given by the squared magnitude of the total amplitude. Phase differences are thus converted into measurable amplitude modulations [55, 54]. Huygens' principle is well illustrated at a grating, as shown in figure 3.1. A plane wave is blocked by an opaque screen except at its slits. There, each opening acts as a source of secondary wavelets whose superposition underlies grating interference.

In the following, these principles are extended to matter waves, where diffraction of metastable helium at nanomechanical gratings serves as a benchmark demonstration

3.1. Kirchhoff–Fresnel theory

Interference phenomena due to diffraction are formally described by the Kirchhoff–Fresnel integral. It applies both to light and to matter-waves, since it requires only a complex-valued wave disturbance U, whose squared magnitude yields the observable intensity $I = |U|^2$. For electromagnetic waves, U corresponds to the electric field amplitude, while for matter-waves it is the wavefunction, with $|U|^2$ interpreted according to Born's rule. In the following, we outline the Kirchhoff–Fresnel theory for diffraction at a screen, with particular emphasis on the far-field limit that is used in Chapter 3.6 to analyze the experimental diffraction of metastable helium. Unless noted otherwise, the derivations follow Born and Wolf [54].

In the Kirchhoff–Fresnel formalism, the general expression for the field at an observation point P is given by:

$$U(P) = -\frac{iA}{2\lambda} \iint_{\mathcal{A}} \frac{e^{ik(r+s)}}{rs} \big(\cos(n,r) - \cos(n,s)\big)\, \mathrm{d}S\,, \tag{3.1}$$

which represents the coherent superposition of all secondary contributions from the spatial elements $\mathrm{d}S$ of an aperture $\mathcal{A}$. Here $k = 2\pi/\lambda$ is the wave number, r and s denote the source-to-

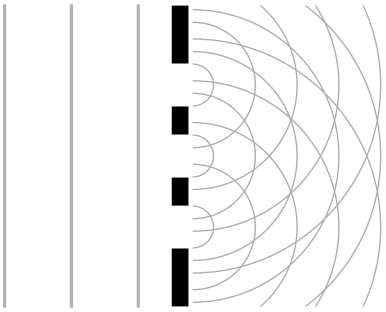

Figure 3.1.: Huygens' principle demonstrated at a grating. Planar wavefronts impinge on an opaque screen with multiple slits, where each opening acts as a point source of circular wavelets. Their superposition lead to the observed interference pattern.

aperture and aperture-to-P distances, n is the aperture surface normal, and A is a constant that depends on the inital amplitude of the diffracted wave.

In the far-field, equation (3.1) simplifies under the condition that both the source and the observation point are far from the aperture compared to its size. For an observation point P close to the optical axis, the factor $\cos(n,r) - \cos(n,s)$ varies only weakly across $\mathcal{A}$ and can therefore be approximated by a constant $2\cos\delta$. Likewise, the term $1/rs$ can be replaced by $1/r's'$, where r' and s' denote the distances from the aperture center to the source and to P. With these approximations, the only significant spatial dependence remains in the phase factor $e^{ik(r+s)}$. Expressing r and s in aperture coordinates (ξ,η) leads to square-root expressions, which can be expanded for small ξ,η relative to r', s'. To first order they are of the form:

$$r + s \approx r' + s' - \left(p\,\xi + q\,\eta\right) + O(\xi^2,\eta^2)\,, \tag{3.2}$$

where p and q denote the direction cosines of the diffracted ray toward P, which in the far-field reduce to the sines of the diffraction angle ϑ, demonstrated in figure 3.5(a). By collecting the contributions with spatial dependence into a general function $f(\xi,\eta) = p\,\xi + q\,\eta + O(\xi^2,\eta^2)$, equation (3.1) simplifies to:

$$U(P) = -\frac{i\cos\delta}{\lambda}\frac{Ae^{ik(r'+s')}}{r's'}\iint_{\mathcal{A}} e^{-ikf(\xi,\eta)}\,\mathrm{d}\xi\mathrm{d}\eta\,. \tag{3.3}$$

Whether quadratic and higher-order contributions of ξ and η can be neglected, or whether $f(\eta,\xi)$ is nonlinear, has direct physical consequences. In the linear case, the integral evaluates purely plane waves. This corresponds to the far-field approximation of wave interference behind a screen, termed Fraunhofer diffraction. Its near-field counterpart, Fresnel diffraction, becomes relevant when the wavefronts are sufficiently curved to influence the interference pattern.

3.2. Fraunhofer diffraction

This section develops the form of interference patterns produced by apertures such as slits and gratings in the far-field limit. This Fraunhofer regime is the one realized in the diffraction

experiments with metastable helium described in 3.6.

Reaching the far-field limit

According to Huygens' principle, the front of a one-dimensional aperture of width η can be treated as an array of point emitters at positions x_s, with $-\frac{\eta}{2} < x_\mathrm{s} < \frac{\eta}{2}$. A point on the detection screen at distance L and transverse coordinate x_p receives contributions from all such emitters. Their corresponding path length is:

$$r_\mathrm{s} = \sqrt{L^2 + (x_\mathrm{p} - x_\mathrm{s})^2} \simeq L + \frac{(x_\mathrm{p} - x_\mathrm{s})^2}{2L} \,. \tag{3.4}$$

This approximation holds when the screen is sufficiently far from the aperture and $(x_\mathrm{p} - x_\mathrm{s}) \ll L$. The quadratic contribution to the phase is then given by:

$$\Phi_\mathrm{s}^{(\mathrm{quad})} = \frac{2\pi}{\lambda} \frac{(x_\mathrm{p} - x_\mathrm{s})^2}{2L} < \frac{\pi\eta^2}{4\lambda L} \,. \tag{3.5}$$

In order for the curvature of the waves to be negligible, their contributions to the phase must be minimal:

$$\frac{\pi\eta^2}{4\lambda L} \ll 1 \,. \tag{3.6}$$

In this limit, the curvature of the wavefront across the aperture is negligible, and the interfering waves can be approximated as planar.

Kirchhoff integral behind an aperture

In the far-field approximation, the phase function $f(\xi, \eta)$ in equation (3.3) simplifies to $f(\xi, \eta) = p\xi + q\eta$, as only plane waves are considered. The Kirchhoff integral therefore reduces to its simplest form:

$$U(P) = C \iint_{\mathcal{A}} e^{-ik(p\xi + q\eta)} \, \mathrm{d}\xi \mathrm{d}\eta \,. \tag{3.7}$$

This integral is functionally equivalent to a Fourier transform of the wave field at the aperture, aside from a constant phase factor C. Consequently, diffraction patterns in the far-field are determined by the Fourier transform of the aperture function. The role of the factor C is to scale the maximum intensity I_0, which occurs at the center of the diffraction pattern, where $p = q = 0$. Its value is given by:

$$I_0 = |U(0,0)|^2 = C^2 D^2 \,, \tag{3.8}$$

where D is the effective aperture area, or width in the one-dimensional case.

3.2.1. Single Slit

An ideal slit can be modeled as a rectangle with one dimension extended to infinity. In this case, diffraction effects arise solely from the finite edges of the aperture, thereby reducing the problem to one dimension. In cases in which the illuminated area of a slit is smaller than its height, this is a reasonable approximation and one whose results agree well with real far-field patterns. For a slit of width $s = 2a$, the corresponding Fraunhofer integral equation (3.7) is:

$$U(p) = C \int_{-a}^{a} e^{-ikp\xi} \mathrm{d}\xi = -\frac{C}{ikp} \left(e^{-ikpa} - e^{ikpa}\right) = C \frac{2a}{2a} \frac{e^{ikpa} - e^{-ikpa}}{ikp} = 2aC \frac{\sin kpa}{kpa} . \tag{3.9}$$

Notably, the dependence of $U(P)$ on P is expressed through $p = \sin\vartheta$, where ϑ is the point's angle relative to the zero-order direction. The observable intensity pattern $I(p)$ is given by the squared magnitude of $U(P(p))$:

$$I(p) = |U(p)|^2 = s^2C^2 \left(\frac{\sin kpa}{kpa}\right)^2 = I_0 \left(\frac{\sin kpa}{kpa}\right)^2 . \tag{3.10}$$

Here, $I_0 = s\mathcal{P}/(\lambda R^2)$, with $\mathcal{P}$ denoting the total power incident on the aperture in the one-dimensional slice A single slit generates an interference pattern proportional to a squared sinc function, with nodes where the wave intensity vanishes. These intensity minima are the zeros of $\sin(kpa)$, found at $kpa = 2\pi n$, and their diffraction angles ϑ_{slit} can be found via p:

$$p = \sin\vartheta_{\text{slit}} = \frac{n\pi}{ka} = \frac{n\pi}{\frac{2\pi}{\lambda}\frac{s}{2}} = \frac{n\lambda}{s} . \tag{3.11}$$

3.2.2. Gratings

A diffraction grating is an arrangement of evenly spaced identical openings that impose a periodic variation of amplitude or phase on an incident wave. At an observation point behind such an arrangement, the converging waves carry amplitudes determined by their respective apertures, along with phase shifts proportional to their relative displacements. The sum over all individual contributions determines the complete intensity pattern. In the Fraunhofer limit, the field $U(p)$ for a one-dimensional grating with N identical slits of width s and periodicity d is given by:

$$U(p) = C \sum_{n=0}^{N-1} e^{-ikp(nd)} \int e^{-ikps} \mathrm{d}s , \tag{3.12}$$

The aperture integral in this equation is the Fraunhofer diffraction integral of a single slit[2]:

$$U^0(p) = \int_{\mathcal{A}} e^{-ikp\xi} \mathrm{d}\xi . \tag{3.13}$$

[2]Technically, the integral that must be considered is of the form $\int_{\mathcal{A}} F(\xi) e^{-ikp\xi} \mathrm{d}\xi$, where $F(\xi)$ is the transmission function of one single element. For an idealized grating made up of perfect single slits $F(\xi) = 1$ is assumed.

This corresponds to the diffracted amplitude contributions of the individual apertures. $U^0(p)$ is a constant, so equation (3.12) becomes:

$$U(p) = U^0(p) \sum_{n=0}^{N-1} e^{-iknd p} = U^0(p) \, \frac{1 - e^{-iNkdp}}{1 - e^{-ikdp}} \, . \tag{3.14}$$

Therefore, the full intensity pattern is:

$$\begin{aligned} I(p) = |U(p)|^2 &= \left(\frac{1 - e^{-iNkdp}}{1 - e^{-ikdp}} \right) \left(\frac{1 - e^{iNkdp}}{1 - e^{ikdp}} \right) |U^0(p)|^2 = \frac{1 - \cos Nkdp}{1 - \cos kdp} \, I^0(p) \\ &= \left(\frac{\sin Nkdp/2}{\sin kdp/2} \right)^2 I^0(p) \, . \end{aligned} \tag{3.15}$$

Without the single-slit factor $I^0(p)$, the expression describes the periodic pattern produced by the array of equally spaced slits. The single-slit term then acts as an envelope that modulates this distribution. Principal maxima occur at $n = Nm$ ($m \in \mathbb{Z}$), where numerator and denominator vanish simultaneously and L'Hôpital's rule yields a finite maximum. Between two such main maxima lie $N - 1$ equally spaced minima of zero intensity.

The angles ϑ_{grat} at which the maxima occur can be found by the same method as for the single slit minima. Maxima occur when $kdp = 2\pi m$, such that:

$$p = \sin \vartheta_{\text{grat}} = \frac{m\pi}{kd} = \frac{m\pi}{\frac{2\pi}{\lambda} d} = \frac{m\lambda}{d} \, . \tag{3.16}$$

The form of these angles closely resemble those of equation (3.11). Comparing both equations shows that for $n/m = s/d$, both angles are the same. Because the individual slit width s must be narrower than the slit separation d, which implies that at intervals of d/s, a grating maximum coincides with a minimum of the slits, thereby suppressing that maximum. Expressing the single-slit contribution $I^0(p)$ explicitly yields the complete grating intensity pattern $I(p)$:

$$I(p) = \frac{s\mathcal{P}}{\lambda R^2} \left(\frac{\sin \frac{Nkdp}{2}}{\sin \frac{kdp}{2}} \right)^2 \left(\frac{\sin \frac{ksp}{2}}{\frac{ksp}{2}} \right)^2 \, . \tag{3.17}$$

Figure 3.5(b) shows the intensity pattern of a grating in the far-field.

3.3. Coherence

All interference patterns considered thus far assume monochromatic waves characterized by a single, fixed wavelength λ. In a spectrum consisting of a range of wavelengths, each monochromatic component produces its own interference pattern. Under ideal conditions, the overall pattern would be the sum of all individual monochromatic contributions. However, in practice, the visibility of the resulting interference pattern depends on several factors, most notably coherence. If the waves are not strictly monochromatic, the relative phase between different wavelets is not

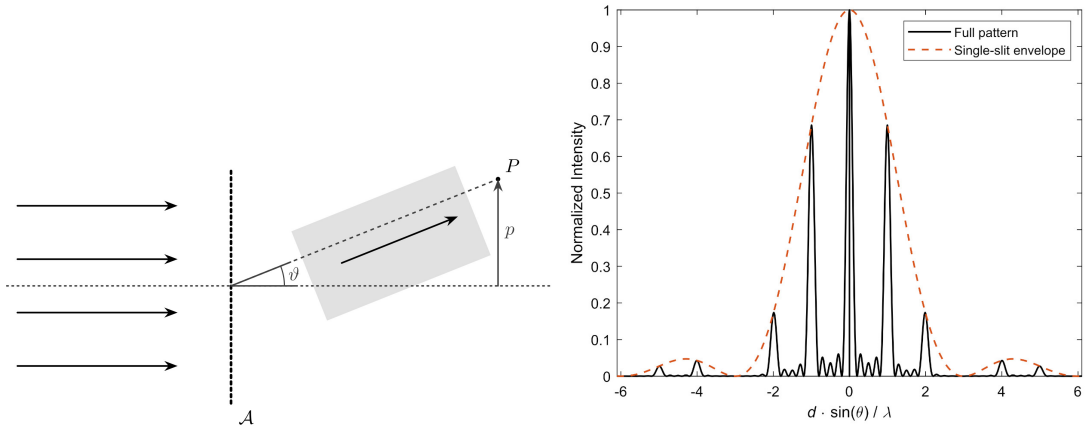

Figure 3.2.: (a) Illustration of the role of $p = \sin\vartheta$ in the far-field. Incoming rays are diffracted at $\mathcal{A}$. At a point P in the far-field, the diffracted rays act as a packet of parallel rays, indicated by the grey region. Adapted from [54]. (b) Ideal far-field diffraction pattern for a wavelength $\lambda = d/100$ and a ratio of $d/a = 3$ between grating period d and slit opening width a. The single-slit contribution acts as enevlope fot the grating pattern and suppresses every third maximum.

constant, but varies over time and hence distance. Consequently, increasing path lengths causes the individual interference patterns to shift relative to one another. With increasing path difference, the individual interference patterns therefore shift relative to one another. This reduces the overall visibility and, in the limit, averages the interference out completely. Waves are considered coherent if their phases remain correlated over a significant period of time. To maintain high interference visibility, the waves must be coherent.

A thorough mathematical description of coherence in polychromatic wave interference must account for the autocorrelation and cross-correlation functions, which describe how individual components of the wave field interact with themselves and with each other. These functions are generally complex-valued, and their form depends on the configuration of the interferometer. In many practical applications, such detailed solutions are not required. Instead, approximations can be made based on simplified assumptions about wave propagation and interaction. Typically, two types of coherence quantifiers are used: longitudinal and transverse coherence lengths.

3.3.1. Longitudinal coherence

The longitudinal coherence length X_L is a measure for the path difference over which interference between two correlated waves remains observable. We consider a source that produces matter-wave beams with mean wavelength λ_0 and spectral width $\Delta\lambda$. The visibility of interference is lost once the phase $\phi = 2\pi L/\lambda$ accumulated over a path length L by a component of wavelength $\lambda_0 + \Delta\lambda/2$ differs by π from that of the central wavelength λ_0. Identifying this path length with X_L leads to

the relation [56]:

$$X_L = \frac{\lambda_0^2}{\Delta\lambda}\left(1 + \frac{\Delta\lambda}{2\lambda_0}\right) \simeq \frac{\lambda_0^2}{\Delta\lambda}\,. \tag{3.18}$$

A narrow velocity distribution therefore directly translates into a longer longitudinal coherence length, allowing interference to remain observable over larger path differences. In optics, longitudinal coherence is commonly introduced via the coherence time $\tau_c = 1/\Delta\nu$, obtained from the spectral width $\Delta\nu$, with X_L then corresponding to the maximum path length traversable during this time. For matter-waves, the propagation speed v is directly linked to the wavelength spectrum, so equation (3.18) provides a more direct definition in terms of the source's velocity spread Δv, as $X_L = \lambda_0^2/\Delta\lambda = \lambda_0\, v/\Delta v$. Alternative approaches, such as assuming Gaussian wave packets and defining $\Delta\lambda$ from the frequency variance via the standard deviation, are also found in the literature. However, in the context of matter-wave interferometry with multiple slits, the relation in equation (3.18) has been shown to agree well with experimental results [56].

3.3.2. Transverse coherence

While the longitudinal coherence length characterizes path differences under which interference arises, the transverse coherence length X_T characterizes the spatial coherence of an extended, partially coherent source by quantifying the phase correlation between two points in space at the same time. Mathematically, this is described by the van Cittert–Zernike theorem. It states that for a quasi-monochromatic, spatially incoherent source observed in the far-field, the first-order spatial coherence between two points x_1 and x_2 is given by a normalized Fourier transform of the source's intensity distribution. This coherence pattern has the same functional form as the Fraunhofer diffraction integral of an aperture whose transmittance equals the source intensity. Hence, the spatial coherence region around a point x_1 can be understood as the aperture's far-field diffraction pattern converging on x_1. This result enables the generation of coherence from initially incoherent illumination, as is common with atomic and molecular sources [55]. By introducing a collimation slit upstream of a grating, the transverse coherence at the grating acquires a sinc profile, as described by equation (3.10). A common estimate of X_T behind a slit is given by the distance between the first-order minima of the diffraction pattern. These minima appear at angles $\pm\lambda/s$ behind a slit of width s. Thus, the transverse coherence length X_T at a distance L is of the form [56]:

$$X_T \sim \frac{L\lambda}{s}\,. \tag{3.19}$$

In matter-wave diffraction, X_T may be interpreted as the region of delocalization, within which it is impossible to determine the precise path taken by the particle. For grating diffraction, the transverse coherence length must be sufficiently large to encompass at least two slits in order for interference to occur. In this context, X_T represents the spatial extent set by the transverse momentum uncertainty in the plane orthogonal to the propagation axis. When a wave passes through a slit of width $s = \Delta x$, the particles acquire a transverse momentum spread Δp_x, as required by the Heisenberg uncertainty relation [57, 56]:

$$\Delta p_x \simeq \frac{h}{\Delta x}\,. \tag{3.20}$$

With this relation, the form of the transverse coherence length from equation (3.19) can be derived heuristically. The particle's acquired transverse momentum uncertainty Δp_x corresponds to the transverse velocity Δv_c. A matter-wave with longitudinal velocity v_z reaches a screen at distance L after a time $t = L/v_z$. The resulting region of transverse uncertainty on the screen, which defines X_T, is then [56]:

$$X_T = \Delta v_x t = \Delta v_x \frac{L}{v_z} = L\frac{\Delta p_x}{p_z} \simeq L\frac{h}{p_z s} = L\frac{\lambda_{dB}}{s} . \tag{3.21}$$

In the case of a collimation slit, this expression acquires an additional prefactor. The far-field diffraction pattern of the slit is a sinc function, whose half width at half maximum (HWHM) corresponds to the diffraction angle $\sin\theta = 0.44, \lambda_{dB}/s$. Accordingly, in the far-field we obtain $\Delta p_x/p_z \approx 0.89 \sin\theta$, and the transverse coherence length is [56, 57, 58]:

$$X_T = \frac{0.89\,\lambda_{dB} L}{s} \simeq \frac{\lambda_{dB}}{\vartheta_{coll}} . \tag{3.22}$$

Here, we identify s/L as the coherence angle ϑ_{coll}.

3.3.3. Coherence in matter-waves

Both longitudinal and transverse coherence depend directly on the absolute de Broglie wavelength $+\lambda_{dB}$. Transverse coherence improves with collimation slits and a greater distance between the diffraction apparatus and the detection plane. Longitudinal coherence can only be enhanced by reducing the velocity spread of the particles. Since the velocity distribution of a particle beam is largely determined by its source, this requires additional velocity selection techniques. A comparatively simple approach is the use of height limiters, which allow particles to be filtered according to their free-fall trajectories [59, 56]. A further option is the use of a beam chopper, where a rotating plate with apertures selectively transmits the beam [60]. However, all such selection methods reduce the overall signal, which makes sources with intrinsically narrow velocity distributions and detectors with high detection efficiency ultimately preferable.

3.4. Gratings for matter-wave interferometry

In the following, we discuss different types of gratings for matter-wave diffraction. We limit the theoretical framework to the eikonal approximation, which treats gratings as thin phase objects that modify only the transverse component of the particle's wavefunction. This approximation is valid if the traversal time through the grating is negligible. It further assumes that the longitudinal and transverse velocities, and hence their associated wavelengths, remain separable throughout the interferometer [61].

In the case of complex molecules, internal states can undergo multiple changes during the diffraction process, which may couple to and affect the center-of-mass motion. Only when these internal dynamics remain decoupled from the center-of-mass motion is interference entire compound's de Broglie wavelength observable [28].

3.4.1. Amplitude and phase gratings in the eikonal approximation

Consider a particle traversing a grating such that only its transverse wavefunction $\psi(x)$ is modulated, while the longitudinal motion along z remains unaffected. Gratings can both absorb intensity and impart a phase shift $\phi(x)$ to the matter-wave. The effect of the grating on $\psi(x)$ is described by a transmission function of the form [61, 28]:

$$\psi(x) \longmapsto t(x)\,\psi(x) = |t(x)|e^{i\phi(x)}\psi(x)\ , \tag{3.23}$$

with the amplitude constrained by $|t(x)| \leq 1$. In the case of a mechanical grating, the bars between the slits correspond to $|t(x)| = 0$. If the particle traverses the grating, $\psi(x)$ is projected onto the slit openings, and the transmitted components subsequently interfere [28].

In a purely amplitude or transmission grating, the complex transmission has uniform phase and imprints no phase modulation on the wavefunction. The transmission is defined solely by its spatial magnitude $t(x) = |t(x)|$. Accordingly, interference arises from free-space propagation, with relative phases accumulating from path-length differences between the transmitting regions and the observation point, as described by the Kirchhoff–Fresnel integral. In contrast, *phase gratings* imprint position-dependent phase shifts onto the wavefunction. The transmission function $t(x)$ then modulates only the phase of the diffracted wave while leaving the amplitude unchanged. Pure phase gratings transmit with 100% efficiency, such that $|t(x)| = 1$. The transmission function $t(x)$ of a grating with period d can be expressed as a Fourier series [61]:

$$t(x) = \sum_{n=-\infty}^{\infty} b_n e^{2\pi i n x/d}\ . \tag{3.24}$$

Applying this expansion to an incident plane wave with transverse phase factor $e^{ip_x x/\hbar}$ yields:

$$t(x)\ \exp\!\left(\frac{ip_x x}{\hbar}\right) \longmapsto \sum_{n=-\infty}^{\infty} b_n \exp\!\left[\frac{i}{\hbar}\left(p_x + n\frac{h}{d}\right)x\right]\ . \tag{3.25}$$

In this picture, the particle's momentum is redistributed, independent of its velocity or mass, in discrete units of the grating momentum $\Delta p_x = h/d$, as a consequence of the uncertainty principle discussed in equation (3.20). Importantly, this redistribution applies equally to amplitude and phase gratings, since it results solely from the periodicity of the transmission function $t(x)$. Diffraction orders therefore correspond to momentum shifts by integer multiples of Δp_x [28].

3.5. Optical gratings

Particle-grating interaction

In realistic diffraction experiments, particles do not interact with the grating solely through geometric transmission or absorption. Instead, additional forces, most notably electromagnetic interactions such as the Casimir–Polder interaction between the particle and the grating material, invariably modulate the wavefunction's phase. These effects become increasingly pronounced for

larger and more complex molecules with higher polarizability [61, 62]. Over typical traversal times of a few nanoseconds, van der Waals interactions with the grating walls can induce phase shifts of several radians in atoms, sufficient to significantly reduce interference visibility [63]. While the influence of these comparatively weak forces can be mitigated using thin membranes or surface coatings, macromolecules with high polarizability, such as typical biomolecules, remain highly sensitive. In such cases, even small residual charges in the grating walls, for example, due to ion beam patterning, can lead to phase averaging and reduced interference visibility [62, 64]. Near the grating walls, interactions may become sufficiently strong that the assumption of separability between longitudinal and transverse motion throughout the whole structure no longer holds. Consequently, the eikonal approximation and its assumption of purely phase-shifting wavefront modulation ceases to be valid [61]. If the van der Waals forces are sufficiently weak to influence only the phase, this can be accounted for by modeling the grating slits with a reduced effective width s_{eff}, a method that has proven successful in noble gas diffraction [65].

Due to the high polarizability of biomolecules, the use of mechanical gratings presents an increasingly significant challenge. For this reason, interferometers designed for such particles typically employ optical gratings as the diffracting element [62, 63].

Light gratings

Optical gratings consist of standing waves of coherent laser light. To first order, the light field induces an electric dipole moment in the particle, which interacts with the resulting potential energy V. Near the grating walls, the potential follows the van der Waals form $V = -C_3/x^3$, while at long range it approaches $V = -C_4/x^4$. The interaction constants C_3 and C_4 are determined by the laser intensity and by the particle's polarizability at the laser frequency. For this reason, optical gratings inherently act as phase gratings. where the electric potential V imprints a position-dependent phase shift $\phi(x) = -1/(\hbar v) \int V(x, z)\, \mathrm{d}z$ onto the diffracted wavefront. The resulting grating period is equal to half the wavelength of the light [61, 65]. However, depending on their interaction with the diffracted molecules, such gratings can also function as amplitude gratings by ionizing or fragmenting particles when the photon energy of the laser beam is sufficiently high. In ionizing gratings, depleted particles are removed from the interferometer before reaching the detector, a technique that has been successfully employed in matter-wave interferometry of large molecules and biomolecules [66, 25, 22]. Pure optical phase gratings have also been employed in matter-wave interferometry [67]. Because the particles interact solely with the laser's electric field rather than with material surfaces, particle-wall interactions are eliminated [61, 63].

Light gratings offer several advantages, as they are indestructible, cannot become clogged, and are perfectly periodic. Moreover, the laser wavelength, and thus the grating period, can be chosen as required and, depending on the laser type, modulated in situ [28].

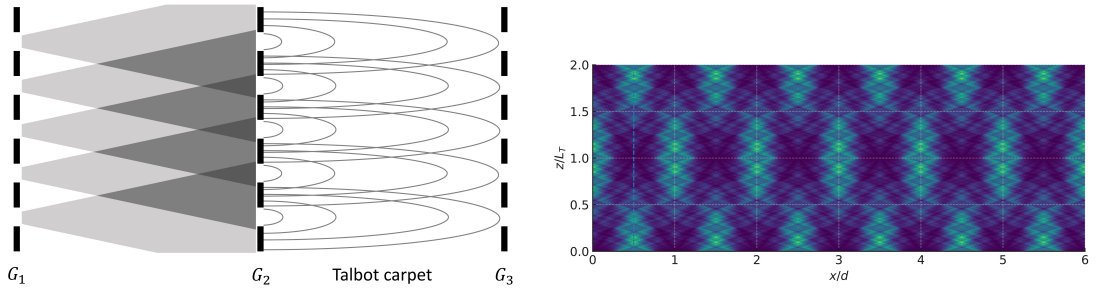

(a)

Figure 3.3.: (a) Talbot–Lau interferometer. G_1 prepares transverse coherence from an initially incoherent beam. G_2 is the source for diffraction, while G_3 samples the resulting fringes in the Talbot carpet. Adapted from [61]. (b) Talbot carpet, the near-field pattern behind a grating. It is characterized by repeated self-images of the grating period d at regular intervals along the beam.

3.5.1. Talbot–Lau interferometry

A major experimental challenge in Fraunhofer diffraction is that the plane-wave assumption is only satisfied for highly collimated beams. Talbot–Lau interferometers instead operate in the near field, where all diffraction orders overlap and interfere. More precisely, coherent illumination of a periodic structure produces a repeating "carpet" of self-images in the near field, a phenomenon known as the Talbot effect, pictured in figure 3.3(b). For a grating with slit separation d, these images recur at integer multiples of the Talbot length L_T, given by [61, 60]:

$$L_\mathrm{T} = \frac{d^2}{\lambda} \,. \tag{3.26}$$

This principle applies to both light and matter-waves. In Talbot–Lau interferometers, three gratings are employed. The first grating collimates the beam and provides sufficient transverse coherence at the second grating, allowing operation even with weakly collimated sources. Near-field diffraction at the second grating generates the Talbot carpet, which is sampled by a third grating with the same period d as the second. This enables scanning of the self-images and leads to a periodic modulation of the detected signal [68, 67, 63].

OTIMA

The Talbot carpet is a spatial phenomenon that can be observed in position space. However, detection can also be performed in the time domain. In the classical limit, the de Broglie wavelength is given by $\lambda_\mathrm{dB} = h/mv$. Substituting this relation into equation (3.26) yields the Talbot time T_T, which is the time required for a particle with wavelength λ_dB to traverse one Talbot length L_T [60]:

$$L_\mathrm{T} = \frac{d^2}{\lambda_\mathrm{dB}} = \frac{mvd^2}{h} \implies T_\mathrm{T} = \frac{L_\mathrm{T}}{v} = \frac{md^2}{h} \,. \tag{3.27}$$

Importantly, the Talbot time T_T is independent of velocity and therefore identical for all particles of equal mass. An interferometer scanning the Talbot time instead of length is thus not intrinsically limited by velocity dispersion [60].

Optical time-domain ionizing matter-wave interferometry (OTIMA) employs three gratings consisting of pulsed standing laser waves and probes transmission resonances as a function of the pulse delay close to the Talbot time. Resonant transmission occurs when the pulse separation matches an integer multiple of T_T, where all particles interact with the same sequence of gratings simultaneously. By varying the pulse separation around this condition, interference is observed as a periodic modulation in the transmission signal contrast [60, 66, 22].

OTIMA has been demonstrated for clusters and polypeptides in the kilodalton mass range using vacuum-ultraviolet (VUV) light [66, 22]. Molecules located at the antinodes are removed from the beam either by ionization or, in the case of fragile clusters, by photofragmentation, while those in the nodes remain as coherent sources of matter-waves. Ions created in this process can be removed by a weak electric field. Neutral fragments, in contrast, may perturb the detected signal unless their size and recoil velocity after dissociation eject them beyond the detector's acceptance angle [25]. For biomolecules efficient ionization at masses $m > 2000\,\mathrm{Da}$ is difficult to achieve, as fragmentation typically dominates over simple ionization [69, 70, 71]. For this reason, a detailed understanding of selective fragmentation processes, as discussed in chapter 4, is essential for the controlled implementation of coherent beam splitters. Tailoring fragmentation at the wavelengths of optical gratings enables a high degree of control over the splitting process, including the molecular charge state and dissociation kinetics [72].

OTIMA therefore represents an important interferometric technique for biomolecular interference. It eliminates the need for material gratings, remains robust against velocity dispersion, and offers a natural pathway toward interference with complex molecular clusters.

3.6. Far-field diffraction of metastable helium

To illustrate the principles of matter-wave diffraction in a concrete setting, we performed far-field diffraction experiments with a beam of metastable helium atoms. The experiment is designed as a model system that captures the essential requirements for observing coherent diffraction of neutral particles. Metastable helium is particularly well suited for such a demonstration as its neutrality allows diffraction to be observed under laboratory conditions without strong perturbations from external fields, while the high internal excitation energy can be measured with a multichannel plate detector (MCP). Here, we therefore describe a proof-of-principle realization of matter-wave diffraction with neutral atoms.

3.6.1. Setup

The full experimental setup is shown in figure 3.4. A beam of metastable helium (He^*) is generated using a cold Even–Lavie valve equipped with a dielectric barrier discharge (DBD). The valve operates at room temperature with a repetition rate of $f = 100\,\mathrm{Hz}$, backing pressure of $p = 50\,\mathrm{bar}$

and pulse durations slightly above $\tau_{\text{pulse}} = 20\,\mu\text{s}$. All measurements are performed under vacuum conditions to suppress velocity broadening and decoherence. The background pressures indicated in figure 3.4 refer to the situation without active valve. During operation, the pressure typically increased by about one order of magnitude. To maintain unperturbed supersonic expansion, τ_{pulse} was adjusted such that the source chamber pressure remained below $p = 10^{-5}$, mbar. The beam is collimated by two slits, S_1 and S_2, before reaching the nanomechanical grating. The nozzle-to-slit distance is approximately 0.5 m, while the separation between S_1 and S_2 is $l_{12} = 0.3\,\text{m}$. The distance from S_2 to the grating is 8 cm, and the grating-to-detector distance is $L = 0.825\,\text{m}$.

Detection is carried out using a Photonis Advanced Performance Long-Life MCP. Its with phosphor screen is read out by an iXon Ultra camera. The MCP's nominal pixel size is $A_{\text{pix}} = 5\,\mu\text{m} \times 6\,\mu\text{m}$. In practice, however, a single detection event consistently triggered signals on multiple adjacent pixels.

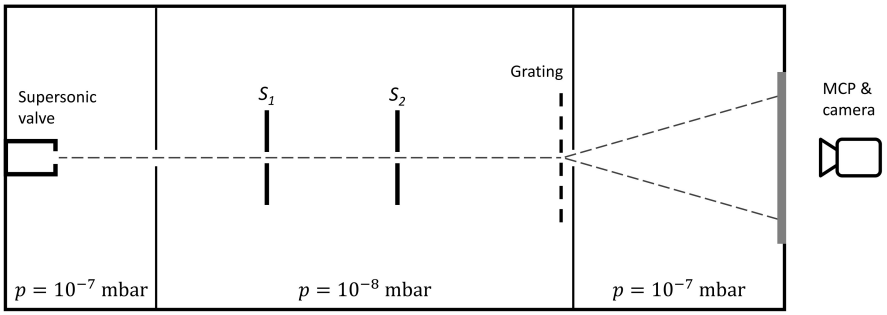

Figure 3.4.: Experimental setup for far-field diffraction of metastable helium. A supersonic beam is collimated by two slits, and transmitted through a nanomechanical grating. Its diffraction pattern is detected at an MCP.

Helium beam

The helium de Broglie wavelength λ_{He^*} and its spectrum $\Delta\lambda_{\text{He}^*}$ are determined by the thermal velocity distribution at the valve. At a room temperature of approximately 300 K, the expected terminal velocity is $v_{\text{He}^*,\text{ex}} \approx \text{per} - \text{mode} = \text{symbol1760}\,\text{m}\,\text{s}^{-1}$, based on equation (5.3). Under comparable source conditions (see section 5.3), with similar pressures and pulse durations, a FWHM velocity spread of about 10% was measured. Using this terminal velocity together with the 10% spread, the expected mean de Broglie wavelength λ_{He^*} and its distribution are:

$$\begin{aligned} \lambda_{\text{He}^*} &= 57\,\text{pm}\,, \\ \Delta\lambda_{\text{He}^*} &= 11\,\text{pm} \approx 0.2\lambda_{\text{He}^*}\,, \end{aligned} \tag{3.28}$$

Grating

Diffraction is performed with a nanomechanical transmission grating consisting of 50 nm thick silicon nitride membranes coated with a 5 nm thin gold layer to suppress charging and reduces

polarization interactions [64]. The grating has a period $d = 100\,\text{nm}$, slit width $s = 45\,\text{nm}$, and $N = 100$ slits. It is mounted on a vertical stage that permits rotation around the vertical axis. The beam is assumed to illuminate the full grating.

Diffraction maxima

From the mean wavelength λ_{He^*}, the expected diffraction angles θ_n follow from equation (3.17). The first-order diffraction angle is:

$$\theta_1 = \frac{\lambda_{\text{He}^*}}{d} = 570\,\mu\text{rad} . \tag{3.29}$$

The corresponding peak separation at the detector located 82.5 cm downstream of the grating is:

$$L\theta_1 = 470\,\mu\text{m} , \tag{3.30}$$

where the small-angle approximation $\sin\theta \approx \theta$ holds.

Collimation slits

To resolve the diffraction peaks, the beam divergence θ_{init} (measured relative to the optical axis) at the grating, must be smaller than the angle to the first diffraction order, $\theta_1 = 570\,\mu\text{rad}$ [73]. With two collimation slits S_1 and S_2 of openings ΔS_1 and ΔS_2 and separated by l_{12}, the acceptance half-angle is:

$$\tan\theta_{\text{init}} = \frac{\Delta S_1 + \Delta S_2}{2l_{12}} . \tag{3.31}$$

Imposing $\theta_{\text{init}} < \theta_1$ yields the maximum combined slit opening for which the diffraction pattern remains resolvable,

$$\Delta S_1 + \Delta S_2 < 2l_{12}\,\tan\theta_1 \approx 2l_{12}\,\theta_1 \approx 342\,\mu\text{m} . \tag{3.32}$$

Each slit consists of a pair of razor blades whose separation is controlled by a piezoelectric actuator.

Calibration of the piezo readings established the maximum closing widths from the zero-transmission settings as $S_{1,x}^{\max} \approx 200\,\mu\text{m}$ for S_1 and $S_{2,x}^{\max} \approx 125\,\mu\text{m}$ for S_2. We assume that for a given setting $S_{i,x}$ the mechanical opening is $\Delta S_i = S_{i,x}^{\max} - S_{i,x}$. The first slit S_1 was operated at $S_{1,x} = 150\,\mu\text{m}$. The second slit S_2 was operated at $S_{2,x} = 97\,\mu\text{m}$. Together, these settings correspond to the opening widths:

$$\begin{aligned} \Delta S_1 &= 50\,\mu\text{m} , \\ \Delta S_2 &= 28\,\mu\text{m} . \end{aligned} \tag{3.33}$$

At the first slit, positioned $\sim 0.5\,\text{m}$ downstream of the $100\,\mu\text{m}$ wide valve nozzle, the transverse coherence length is $X_T \simeq 285\,\text{nm}$, which is smaller than ΔS_1 by roughly two orders of magnitude. Accordingly, the beam incident on S_1 is effectively incoherent, and S_1 acts as the coherent source for the interferometer. The second slit S_2, located $l_{12} = 30\,\text{cm}$ downstream of S_1, selects the collimation angle θ_{init} as defined above. These opening values also satisfiy the collimation angle condition given in equation (3.32).

Coherence lengths

The longitudinal coherence length is set by the wavelength spread:

$$X_{\mathrm{L}} = \frac{\lambda^2}{\Delta\lambda} \approx 3\,\text{Å} \approx 5.3\lambda_{\mathrm{He}^*} \,. \tag{3.34}$$

Transverse coherence is prepared by the first slit, which has an opening width of $\Delta S_1 = 50\,\mu\text{m}$ and is positioned at a distance $l_s = 40\,\text{cm}$ upstream of the grating. The transverse coherence X_{T} at the grating is therefore:

$$X_{\mathrm{T}} = \frac{0.89\lambda_{\mathrm{He}^*} l_s}{\Delta S_1} \approx 406\,\text{nm} \approx 4d \,. \tag{3.35}$$

Thus, more than one grating period is coherently illuminated, enabling multi-slit diffraction. The number N of slits covered by X_{T} is given by $N = 1 + d/100\,\text{nm}$:

$$N = 5 \,. \tag{3.36}$$

In the diffraction analysis, N is included as a fit parameter as a consistency check on this estimate.

Validity of far-field limit

equation (3.6) describes the conditions under which the far-field limit can be applied. We take the aperture to be the coherently illuminated region of the grating with $\eta = 4d$ and obtain:

$$\frac{\pi\eta^2}{4\lambda_{\mathrm{dB}}} = 0.2\,\text{cm} \ll L = 82.5\,\text{cm} \,. \tag{3.37}$$

The condition is satisfied and the experiment operates in the far-field limit.

Modeling of expected diffraction pattern

In theory, the expected far-field diffraction pattern is given by equation (3.17). However, because the source is not perfectly monochromatic, this pattern is broadened by the spectral distribution of de Broglie wavelengths around the mean velocity. Moreover, metastable helium in the $2,^3S_1$ state carries a magnetic dipole moment due to its spin-triplet character. Since this state has no orbital angular momentum, it possesses no permanent electric dipole moment. However, polarization effects may be induced when the atoms interact with the electric potentials near the grating walls [65].

To account for these deviations, the theoretical diffraction pattern is broadened by incorporating the velocity distribution of the atoms. The resulting intensity profile is subsequently convoluted with a Gaussian kernel that models incoherent contributions [74]. The complete fitting function, described in detail in Appendix A, contains as free parameters the mean de Broglie wavelength λ_{He^*}, its spectral width $\Delta\lambda_{\mathrm{He}^*}$, the collimation parameter σ_{coll}, the effective slit width s_{eff}, and the number of coherently illuminated slits N.

Table 3.1.: Fitted diffraction parameters for metastable helium with fit quality $R^2 = 0.968$. The mean velocity v_{He^*} and velocity spread Δv_{He^*} are calculated from the obtained de Broglie wavelength values.

Parameter	Symbol	Value	Unit
Mean wavelength	λ_{He^*}	56.0 ± 0.2	pm
Spectral width	$\Delta\lambda_{He^*}$	12.8 ± 0.8	pm
Collimation parameter	σ_{coll}	117.0 ± 1.0	µm
Effective slit width	s_{eff}	34.3 ± 0.2	nm
Illuminated slits	N	5	–
Mean velocity	v_{He^*}	1780 ± 6	m/s
Velocity spread	Δv_{He^*}	407 ± 25	m/s

Table 3.2.: Measured peak-to-peak spacings of the diffraction pattern. Values are given for negative ($-m$) and positive ($+m$) diffraction orders. A small left–right asymmetry of about 0.6% is observed.

Order m	Δx_{-m} (µm)	Δx_{+m} (µm)
1	460.6	463.5
2	915.1	921.1

3.6.2. Results & discussion

The measured diffraction pattern is shown in figure 3.5 together with the fitted model curve. The fit reproduces the observed intensity distribution with high accuracy ($R^2 = 0.968$), as listed in table 3.1). The mean de Broglie wavelength obtained by the fit $\lambda_{He^*} = (56.0 \pm 0.2)$ pm agrees well with the value expected from the thermal velocity distribution of the Even–Lavie valve, confirming that the source and collimation scheme provide sufficient spatial and temporal coherence to illuminate multiple grating slits coherently. The observed relative velocity spread $\Delta v_{He^*}/v_{He^*} \approx 0.23$ is significantly larger than the performance typically achieved by the Even–Lavie valve under high-vacuum conditions [33]. During the experiment, pressures in the source chamber occasionally exceeded $p = 10^{-5}$ mbar, where collisions with residual gas are expected to contribute to the additional broadening of the velocity distribution.

The fitted effective slit width s_{eff} is smaller than the nominal fabrication value, consistent with atom-surface interactions that have also been observed in helium diffraction at nanomasks [65]. Notably, the visibility of the second diffraction orders indicates that the effective open fraction s/d is closer to 0.33 than to the nominal ~ 0.45. At the larger nominal value, the second orders would be strongly suppressed.

Table 3.2 lists the measured peak-to-peak separations of the diffraction orders. The values agree well with the predicted spacing and reveal a small but systematic left–right asymmetry of approximately 0.6%, consistent across both the first- and second-order diffraction peaks. This asymmetry most likely originates from a slight misalignment of the grating with respect to the beam axis or from residual imperfections in the grating structure. Phase shifts induced

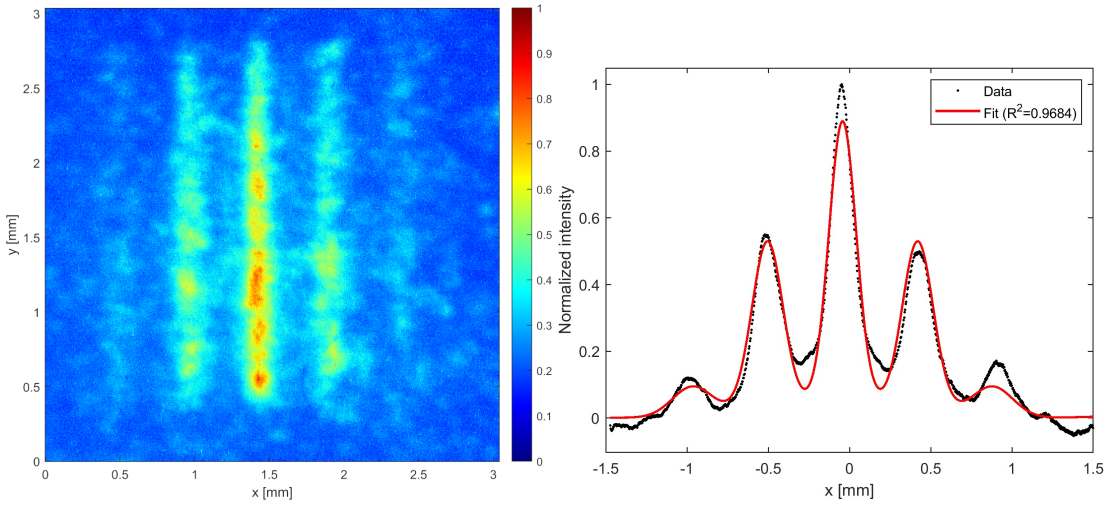

(a)

Figure 3.5.: Far-field diffraction of metastable helium at the nanomechanical grating. (a) Image of the interference pattern at the MCP obtained by the iXon Ultra camera, normalized between 30–70% of the maximum intensity to suppress noise and enhance contrast. (b) Vertically integrated intensity profile (black) with fitted model (red). First- and second-order peaks are clearly resolved, which supports the effective open fraction of $s_{\mathrm{eff}}/d \approx 0.33$ found by the fit.

by parabolic free-fall displacement of the beam trajectory could, in principle, be measured by introducing height limiters and varying the beam inclination [59], but such effects are not relevant in the present case due to the absence of height limiters. The fitted broadening of the diffraction peaks is in good agreement with the expected spectral distribution of the beam.

In future applications, metastable helium produced by an Even–Lavie valve could serve as a well-characterized reference beam for the calibration and alignment in protein interferometers.

4. Photocleavage

Photon-induced ionization and fragmentation can serve as effective beam splitters for complex molecules. Optical beam splitters rely on the controlled removal of particles at the antinodes of a standing light wave, but for many biomolecules the ionization cross section at VUV photon energies is too small for efficient depletion [25]. Most biomolecules require absorption of more than one VUV photon to ionize [75]. In multiphoton processes, the excess energy is often redistributed, which leads to fragmentation rather than clean ionization. In such cases, the resulting fragments recoil out of the forward-propagating beam, thereby realizing an effective absorptive grating, a process shown in figure 4.1.

This chapter introduces the principles of photocleavage, describes the experimental implementation with a ruthenium complex, and extracts the corresponding cross sections as mechanisms to control molecular motion and charge. Ruthenium complexes serve as model systems because their well-characterized photochemistry provides a suitable testbed for studying the interplay between bond cleavage and charge redistribution.

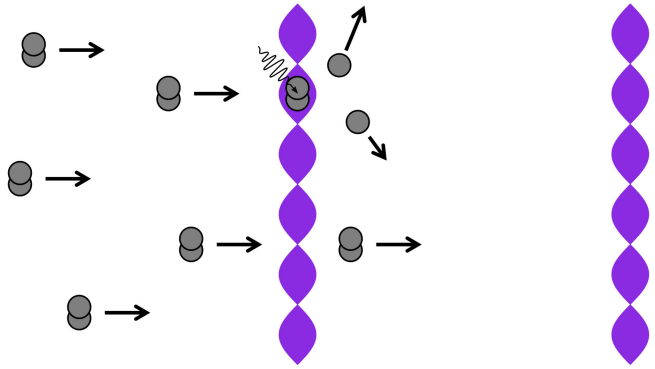

Figure 4.1.: Operating principle of a fragmentation grating. A beam of clusters (sketched as two bound particles) is incident on a standing-wave light field. Trajectories through intensity nodes leave the center-of-mass momentum unchanged, while passages through anti-nodes lead to photon absorption and fragmentation. The fragments depart with a broad, diffuse momentum distribution and are effectively removed from the coherent beam. Adapted from [25].

4.1. Photoabsorption and de-excitation processes

When an atom or molecule absorbs a photon, it is excited to a higher electronic state, specifically one or more electrons are promoted into a higher-energy orbital [76]. In order to optimize energy, electrons tend to dissipate the excess energy and eventually return to the ground state. Depending on the structure of the compound, there are several relaxation pathways an excited electron can follow. These processes are classified as *photophysical* or *photochemical*, depending on whether they return the particle to its original state or result in a permanent chemical alteration [76, 77].

Photophysical processes

Photophyscial processes encompass both radiative and nonradiative transitions. Resonance radiation is the simplest case of emission in that the electron returns directly to its original state while emitting a photon with the same wavelength as the one absorbed. However, in molecules, especially complex ones, resonance emission is typically negligible, because the absorbed energy is rapidly redistributed through other pathways [78, 76]. Orbitals of higher energy generally have larger average radii, so electronic excitation shifts the electron density farther from the nucleus. This weakens the overall binding strength, effectively releasing part of the system's potential energy given by the Coulomb attraction. The Franck–Condon principle states, that changes between electronically excited states are $\approx 10^2$-times faster than nuclear motion. As the nuclei relax to the new electronic configuration, the excess energy is usually converted into vibrational modes around the new equilibrium points. Electronic excitations are therefore likely to result in vibrationally excited states [77]. From there, the dominant pathways back to the ground state are fluorescence, phosphorescence, internal conversion, and intersystem crossing. Figure 4.2 shows a Jablonksi diagram demonstrating the different possible pathways.

Intersystem crossing (ISC) describes a transition between vibrational levels of comparable energy belonging to electronic states of different spin multiplicities [79]. Pathways that return the electron to the ground state without spin flips are known as internal conversion (IC), or more generally as nonradiative (NR) decay [77]. Vibrational relaxation is typically quenched rapidly in solution by collisions. In molecular beams, where collisions are absent, relaxation occurs solely through intramolecular vibrational redistribution (IVR). Typical IVR timescales are slower than collisional vibrational relaxation but still on the order of picoseconds, corresponding to rate constants of $k_{\mathrm{IVR}} \sim 10^{11}\text{–}10^{12}\ 1/\mathrm{s}$, and remain faster than all competing electronic transitions [80]. By comparison, internal conversion typically occurs with rates of $k_{\mathrm{IC}} \sim 10^{9}\text{–}10^{12}\ 1/\mathrm{s}$, while intersystem crossing proceeds more slowly, in the range of $k_{\mathrm{ISC}} \sim 10^{6}\text{–}10^{9}\ 1/\mathrm{s}$, depending on molecular structure and spin-orbit coupling strength. Consequently, subsequent electronic processes generally originate from the vibrational ground state of the electronically excited level [77, 81]. Nonradiative rate constants between two states generally scale inversely with their energy separation, a relation known as the energy gap law [82].

Radiative decay pathways return the excited electron to the ground state through the emission of a photon. In fluorescence, the transition occurs directly from an excited singlet state to the singlet ground state. Phosphorescence emission is preceded by intersystem crossing and thus

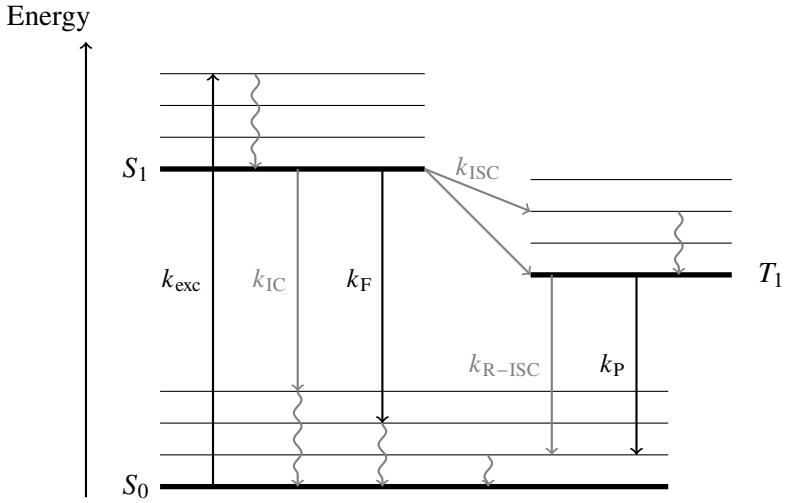

Figure 4.2.: Jablonski diagram of relaxation pathways. Excitation (k_{exc}) promotes the system into an excited state. Relaxation occurs via vibrational relaxation, internal conversion (k_{IC}), fluorescence (k_{F}), intersystem crossing (k_{ISC}), reverse intersystem crossing ($k_{\mathrm{R-ISC}}$), and phosphorescence (k_{P}). Black arrows indicate radiative processes, gray arrows non-radiative transitions, and wavy arrows vibrational relaxation. Adapted from [77]

constitutes a transition from a triplet to a singlet state. Due to the Franck–Condon principle, the transition typically ends in a vibrationally excited level of the electronic ground state. Characteristic fluorescence lifetimes are on the order of nanoseconds, corresponding to rates of $k_{\mathrm{F}} \sim 10^7 - 10^9$ 1/s, whereas phosphorescence is typically much slower, with rates of $k_{\mathrm{P}} \sim 10^0 - 10^4$ 1/s depending strongly on spin-orbit coupling [76, 78, 81].

Photochemical processes

Photochemical processes include ionization, photoisomerization, and photofragmentation, also referred to as photodissociation or photocleavage, which is the main focus in this chapter.

Ionization occurs when the absorbed photon energy exceeds the electron's binding energy, resulting in its removal from the molecule. Photoisomerization, by contrast, refers to an absorption-induced change in molecular configuration. Typical mechanisms include promotion of an electron from a bonding to an antibonding orbital or the partial breaking of a double bond. These alterations of the electronic and spatial bond distribution enable intramolecular rotation. After relaxation, the molecule adopts a different isomeric form, such as a transition from a cis- to a trans-configuration [76, 78].

Photocleavage

Photodissociation is the irreversible breaking, or cleavage, of a chemical bond in a molecule, induced by the absorption of one or more photons. To successfully cleave, the absorbed energy must at least exceed the binding energy of the weakest bond in the molecule [78]. After photon absorption, the energy is internally converted and there may be several internal processes before cleavage occurs. Cleavage processes are typically classified as either homolytic or heterolytic, depending on how charges are distributed onto the fragments. In homolytic fragmentation the electrons are distributed equally, resulting in the formation of two radicals. Heterolytic cleavage leaves behind two ions of opposite charge [45, 83].

4.2. Phototags

Photocleavable tags, also known as photocages, are molecular subgroups that can be selectively removed through a photodissociation process. Especially relevant for matter-wave interferometry is the ability to control the charge of the resulting fragments. Tailored tags can remove charges bond-specifically [84], and have been shown to reduce the charge states of peptides and even neutralize insulin ($m \approx 5800\,\mathrm{Da}$) [45]. These processes can be controlled due to the high spatial and temporal precision of pulsed laser light [72]. Exact dissociation channels are molecule-specific and depend on the structure of the tag, or leaving group (LG) itself [83].

4.2.1. Ruthenium complexes

The photoabsorption behavior of ruthenium complexes in solution has been extensively studied, with well-characterized photophysical properties and photoreactivities [85, 86].

Figure 4.3 shows a Jablonski diagram of the ligand dissociation mechanism. Upon photon absorption, the dissociative Ru-L bond is excited from the singlet ground state ^{1}GS to the singlet metal-to-ligand charge-transfer state ^{1}MLCT. This state undergoes ultrafast intersystem crossing ($< 50\,\mathrm{fs}$) to the triplet ^{3}MLCT state, which serves as the effective starting point for ligand dissociation. From there, photophysical return to ^{1}GS can occur via the radiative and nonradiative pathways discussed above, while the fragmentation pathway proceeds through thermal population of a dissociative ligand field ^{3}LF state [85]. This state's state is characterized by antibonding orbitals, whose occupation destabilizes the Ru-L bond and thus promotes cleavage. Population of ^{3}LF depends on the activation barrier E_a, determined by the relative energies of ^{3}MLCT and ^{3}LF as well as the nuclear displacement and electronic coupling between the respective potential energy surfaces [86]. The chemical structure of the ligand plays a decisive role, as weakly bound ligands dissociate readily, whereas strongly bound ligands require geometric distortions to sufficiently lower the ^{3}LF energy. Moreover, nonradiative decay of ^{3}MLCT follows the energy gap law, such that smaller energy gaps accelerate relaxation directly to the ground state and thereby limit photoreactivity. The competition between these pathways ultimately determines the quantum yield of ligand dissociation [85, 86].

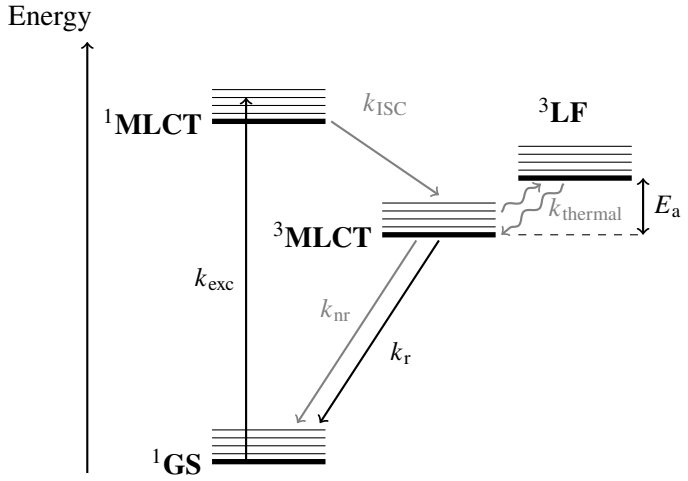

Figure 4.3.: Jablonski diagram showing of the photodissociation path in a Ru(II) polypyridyl complex. Photoexcitation populates the ^{1}MLCT state, which undergoes intersystem crossing to ^{3}MLCT. This state can relax to the ground state either radiatively (k_r) or nonradiatively (k_{nr}). Alternatively, thermal population of the dissociative ^{3}LF state promotes ligand release. Adapted from [85].

Experimental design

The photophysical properties of ruthenium–pyridyl complexes depend strongly on the ligand, whose choice tunes the activation barrier E_a and photoreactivities at different wavelengths [85].

Section 4.4 discusses the experimental findings for $[Ru(tpy)(acac)L]^+$, a ruthenium(II)-based coordination complex functionalized pyridinium ligand, fully shown on the left in figure 4.4. The complex was studied under varying laser power levels to evaluate photodepletion efficiency and dissociation characteristics. The whole compound has a mass of $m = 767.2$ Da and is launched into the gas phase via electrospray ionization (ESI) with a charge of $z = +1$. Its proposed dissociation pathway is shown in figure 4.4. Photon absorption at a wavelength of $\lambda = 355$ nm cleaves the bond between ruthenium and the ligand, which neutralizes the ligand fragment with $m = 332.2$ Da. The remaining charged ruthenium(II) complex, $[Ru(tpy)(acac)]^+$ ($m = 434.0$ Da), can also undergo cleavage upon absorption of 355 nm light, releasing a neutral acetylacetonate (acac) group and the remaining charged $[Ru(tpy)]^+$ complex with $m = 335$ Da. This final step is associated with a formal reduction of the metal center from ruthenium(II) to ruthenium(I).

4.3. Photodissociation cross section

Photon absorption by a molecule results in an increase in the total energy of the molecular state. If this energy exceeds the binding energy of at least one bond, cleavage pathways become accessible [78]. We consider a number N of precursor molecules exposed to a laser pulse of

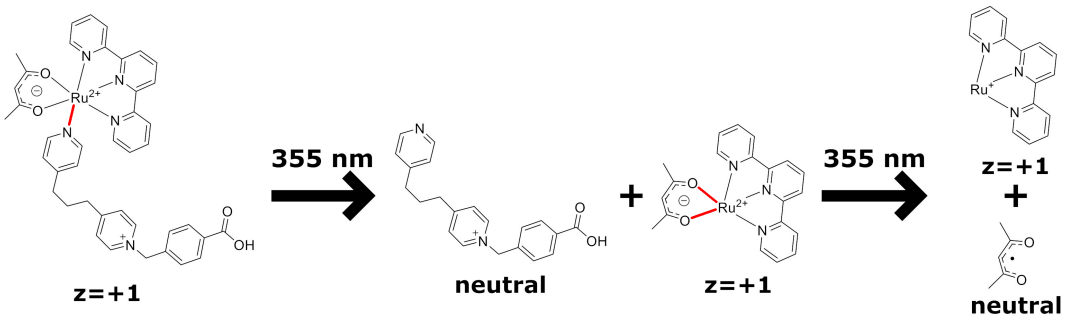

Figure 4.4.: Proposed photodissociation pathway of $[Ru(tpy)(acac)L]^+$ upon irradiation with a wavelength of $\lambda = 355\,\mathrm{nm}$. Bonds proposed to cleave are highlighted in red, while the formal charge of each species is indicated in text.

duration $\mathrm{d}t$, frequency ω, and photon flux ϕ, defined as the number of photons per unit area and time. The resulting signal decrease $\mathrm{d}N$, corresponding to the loss due to fragmentation, is then given by [87]:

$$\frac{\mathrm{d}N}{\mathrm{d}t} = -\sigma_\mathrm{p}(\omega)\phi N \,. \tag{4.1}$$

This treatment assumes a one-photon decay process. The photodissociation cross section $\sigma_\mathrm{p}(\omega)$ denotes the fraction of the total absorption cross section that leads to dissociation. Although excitation by a photon of energy $\hbar\omega$ promotes the molecule to a higher state, not all decay paths might lead to cleavage. Consequently, $\sigma_\mathrm{p}(\omega)$ is generally smaller than the full absorption cross section. By integrating equation (4.1), we obtain the depletion rate N/N_0:

$$\frac{N}{N_0} = e^{-\sigma_\mathrm{p}(\omega)F} \,, \tag{4.2}$$

where N_0 is the initial number of precursor molecules and $F = \phi t$ is the fluence, i.e. the number of photons per unit area during the interaction time. For a pulsed laser, the fluence per pulse is given by:

$$F = \frac{E_\mathrm{p}}{\hbar\omega A} = \frac{1}{\pi hc}\frac{\lambda E_\mathrm{p}}{r_\mathrm{eff}^2} \,, \tag{4.3}$$

where E_p is the pulse energy, $A = \pi r_\mathrm{eff}^2$ the effective beam area, ω the photon angular frequency, and $\lambda = 2\pi c/\omega$ the corresponding wavelength.

equation (4.2) is effectively a modified Beer–Lambert equation, which makes it possible to infer cross sections $\sigma_\mathrm{p}(\omega)$ at a laser frequency ω from fragmentation rates at different pulse energies. Under experimental conditions, an additional factor α needs to be introduced to account for the geometrical overlap between molecular beam and laser profile [88]:

$$\frac{N}{N_0} = 1 - \alpha + \alpha e^{-\sigma_\mathrm{p}(\omega)F} \,. \tag{4.4}$$

Depending on the binding energies, molecules may need to absorb more than one photon to reach the dissociation threshold. If a fraction $(1-\gamma)$ dissociates after absorption of a single photon, the remaining fraction $0 < \gamma < 1$ will need to absorb at least two photons. This adds an additional fluence dependent term in equation (4.4) [88]:

$$\frac{N}{N_0} = 1 - \alpha + \alpha(1 + \gamma\sigma_\mathrm{p} F)e^{-\sigma_\mathrm{p}(\omega)F} \,. \tag{4.5}$$

Based on previous measurements at a wavelength of $\lambda = 450\,\mathrm{nm}$, the photodissociation cross section σ_p of $[\mathrm{Ru(tpy)(acac)L}]^+$ in aqueous solution can be inferred to be[3] [85]:

$$\sigma_\mathrm{p}(450\,\mathrm{nm}) \simeq 3.8 \times 10^{-17}\,\mathrm{cm}^2 \,. \tag{4.6}$$

4.4. Photocleavage

4.4.1. Setup

The goal of the setup is to induce photocleavage in a beam of ESI launched $[\mathrm{Ru(tpy)(acac)L}]^+$ compound, whose structure is shown in figure 4.5, measure its depletion efficiency and check whether the fragmenation path is the one proposed in section 4.2.1. This is achieved by exposing an ESI launched ion beam to an antiparallel laser beam. It is detected by a customized Waters Q-TOF Ultima mass spectrometer. Photodepletion efficiency is quantified by comparing the intensity of the parent ion signal in the mass spectrum at various pulse energies.

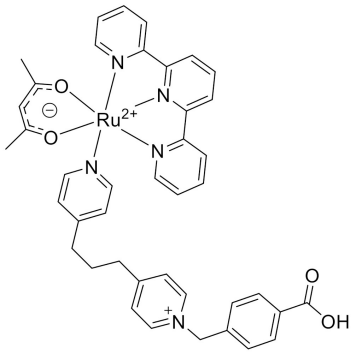

Figure 4.5.: The investigated $[\mathrm{Ru(tpy)(acac)L}]^+$ compound.

The whole setup is shown in figure 4.6. After being ESI launched, ions are guided into the TOF chamber. Photodepletion is modeled by equation (4.5), such that the fit parameters are the spatio-temporal beam overlap α between the laser and ion beam, the ratio of multi-photon (i.e. non single-photon) processes γ, the laser fluence ϕ, and the depletion cross section σ_p at the laser wavelength $\lambda = 355\,\mathrm{nm}$.

[3]This value of the photodissociation cross section σ_p was inferred by equating the exponential decay law obtained from the Arrhenius lifetime analysis in [85] with the depletion law given in equation (4.4), using the reported pulse parameters to estimate the photon fluence.

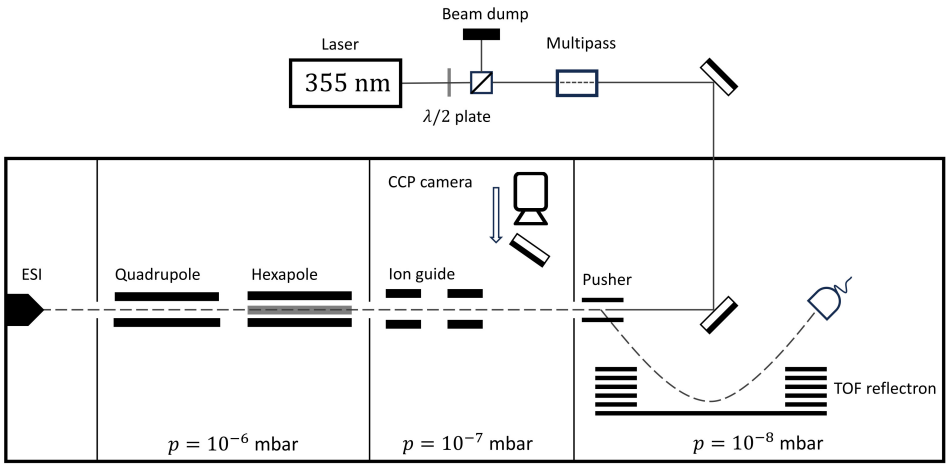

Figure 4.6.: Experimental setup for photocleavage measurements of [Ru(tpy)(acac)L]. Ions are generated by electrospray ionization (ESI), guided through ion optics, and analyzed in a TOF mass spectrometer. A homogenized laser beam is aligned to overlap with the ion beam in the interaction chamber. A CCD camera can be positioned in front of the TOF entrance aperture to record the laser beam profile.

Ion beam

The ruthenium complexes are prepared by electrospray ionization, skimmed at the counter-electrode and collimated and held on axis with an RF ion funnel behind the first differential pumping stage. They are are then pre-selected by the mass spectrometer's quadrupole mass filter, which is 20 cm long and has a resolution of 2000 : 1, with a detection range up to $m/z < 30\,000$ Da/e. A hexapole then guides the ions to a second pumping stage. At this point, the pressure is around $p = 10^{-6}$ mbar. After traversing the pumping stage, the beam guided into the TOF chamber by four stacks of DC ring electrodes. These are arranged in such a way that two of them are always zipped against each other, resulting in two electrode tubes, which are mounted directly behind each other.

Laser

An Innolas SpitLight EVO I, a diode-pumped pulsed Nd:YAG laser, serves as laser source and is operated at the frequency tripled wavelength of $\lambda = 355$ nm, matching the electronic absorption maximum of the compound at approximately 370 nm [86]. The fluence F of a laser pulse with energy E_p is given by equation (4.3). Here, we choose the effective beam radius r_eff such that it contains 95% of the total intensity.

To have better control over the pulse energies, a $\lambda/2$ plate is followed by a polarizing beam splitter (PBS), which redirects one polarization component into a beam dump. This makes it possible to select any energy from zero to the maximum for the of depletion curve. Guiding the light through the multipass arrangement, consisting of two mirrors, increases the optical path

length and allows the beam to approach the far-field regime, where diffraction averages over fine-scale irregularities of the near-field distribution and results in a smoother transverse intensity profile [54]. Subsequently, the laser is directed into the TOF-MS chamber, where it is reflected to overlap parallel to the ion beam. The laser is operated at a repetition rate of $f_{\mathrm{rep}} = 10\,\mathrm{Hz}$, while the TOF pusher is driven at twice this frequency $f_{\mathrm{TOF}} = 20\,\mathrm{Hz}$. Under these conditions, every second TOF sweep exhibits no measurable depletion, irrespective of the incident laser power. This ensures that each depletion event corresponds to the interaction with a single laser pulse.

Beam profile

Efficient molecular beam depletion requires a high spatial overlap α between the molecular and laser beams. Thus, a flat-top laser profile is desired, as it ensures uniform power distribution across the entire ion beam cross-section. Because the ion–laser interaction occurs before the ions enter the mass spectrometer, the laser passes through the TOF entrance aperture, where Fresnel diffraction can significantly modulate its intensity profile. Measurements with a CCD camera at various distances from the aperture showed that several centimeters downstream, the resulting Fresnel rings led to intensity variations of about 20% around the mean level, while near the interaction region these effects were much less pronounced. In this region, the beam exhibits a quasi-flat-top intensity distribution, as shown in figure 4.7(a). The image shows the temporal average of all video frames recorded over 50 s. From this map, the azimuthally averaged radial profile, shown in figure 4.7(b), is obtained by averaging pixel values in concentric rings around the refined beam center. The beam energy as a function of radius is calculated from the cumulative sum of the ring intensities. We definde the effective radius r_{eff} as the radius enclosing 95% of the total energy. Its value is:

$$r_{\mathrm{eff}} = (1.96 \pm 0.05)\,\mathrm{mm}\,. \tag{4.7}$$

After characterizing the beam profile, the CCD camera was replaced with a pulse energy meter so that fluence values for the depletion curve measurements could be obtained.

Conducting the experiment

A beam of [Ru(tpy)(acac)L] molecules is generated by ESI in positive mode. The laser energy is varied in 13 steps via the $\lambda/2$-plate. TOF-MS sweeps alternate between ions exposed to the laser and reference ions without laser interaction, enabling determination of the relative depletion rate for each sweep individually. From these measurements, the photocleavage parameters of the molecule are derived.

4.4.2. Results & discussion

Depletion

Figure 4.8(a) shows the obtained TOF mass spectrum, where the main peak is found at $m/z = 767.2\,\mathrm{Da/e}$, corresponding to the uncleaved $[\mathrm{Ru(tpy)(acac)L}]^+$. Additional peaks were measured at mass values of $m/z = 434\,\mathrm{Da/e}$ and $m/z = 335\,\mathrm{Da/e}$. These peaks correspond to the predicted

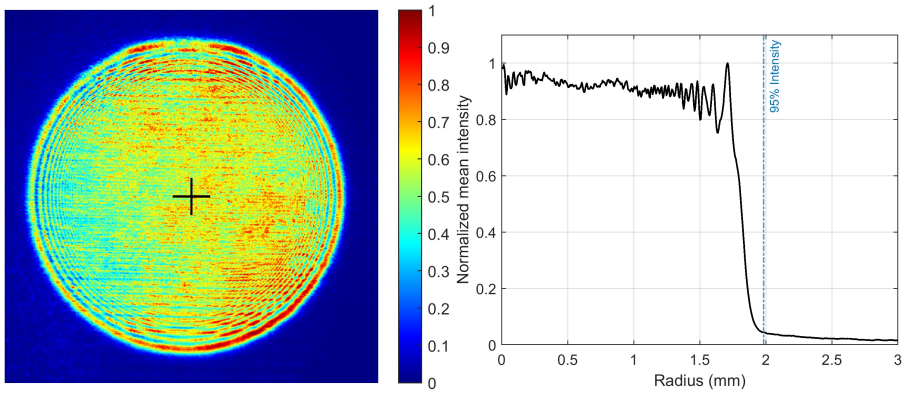

(a) (b)

Figure 4.7.: Measurement of the laser beam profile behind the TOF entry aperture. (a) Heatmap of the beam profile, obtained by averaging all video frames recorded over 50 s. A black cross marks the refined beam center. (b) Azimuthally averaged radial intensity, computed from (a). The dashed line marks r_{eff}, the radius enclosing 95% of the encircled energy.

charged fragments as shown in figure 4.4. The $m/z = 335\,\text{Da/e}$ is accompanied by another peak at $m/z = 347\,\text{Da/e}$, which does not correspond to any proposed fragment. Figure 4.8(b) displays the depletion curve of the main peak at $m/z = 767.2\,\text{Da/e}$, whose fit yields the values:

$$\begin{aligned} \sigma_{\text{p}} &= (4.30 \pm 0.84) \times 10^{-17}\,\text{cm}^2\,, \\ \gamma &= (86 \pm 10)\,\%\,, \\ \alpha &= 100_{-11}\,\%\,. \end{aligned} \tag{4.8}$$

A beam overlap of $\alpha \approx 1$ reflects good alignment in the experimental setup.

The measured absorption cross section is slightly larger than the value obtained for the compound in solution, as calculated in equation (4.6). Given that both the molecular environment and the fragmentation pathways differ in our experiment, this agreement cannot be taken as evidence for a true correspondence. It may suggest that the diffracting ^{3}LF state is populated to a comparable extent. According to the high value of γ, the absorption appears to be two-photon process.

The presence of the ion fragments in the mass spectrum at the predicted masses, along with the absence of fragments at different m/z values, demonstrates that efficient charge control and neutralization of fragments is possible with the proposed method. This enables selective neutral dissociation of tailored ligands, as well as single electron oxidation and reduction. Charge-state control has broad utility for molecular trapping, optical spectroscopy, and mass spectrometry, while reactive metal uncaging is relevant to phototherapy, where the strong absorption of ultraviolet light in tissue limits penetration depth [85].

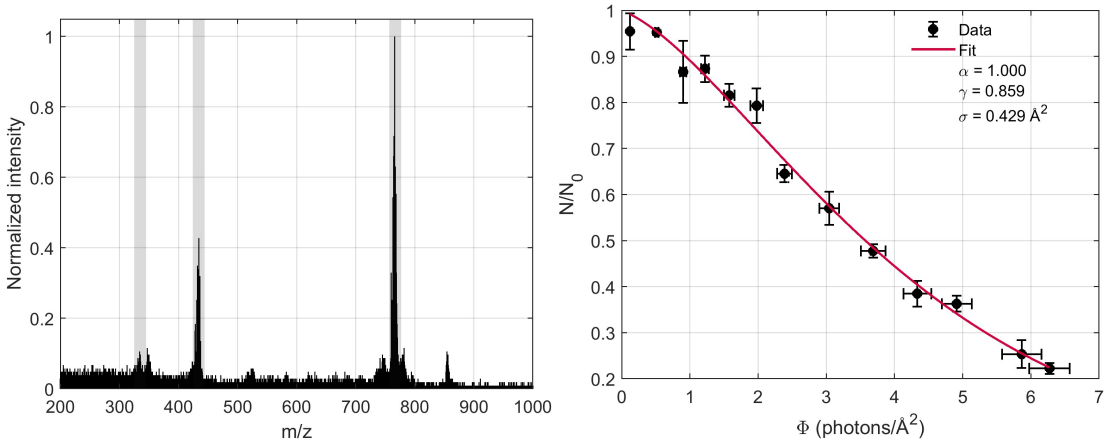

(a) (b)

Figure 4.8.: TOF mass spectrum of $[Ru(tpy)(acac)L]^+$ during the depletion experiment at a wavelength of $\lambda = 355\,\text{nm}$. The main peak at $m/z = 767.2\,\text{Da/e}$ corresponds to the undepleted compound, while peaks at $m/z = 434\,\text{Da/e}$ and $m/z = 335\,\text{Da/e}$ correspond to ion fragments in the proposed fragmentation pathway. These peaks are highlighted within a $\pm 10\,\text{Da/e}$ window. (b) Relative depletion of the parent ion as a function of laser fluence, proportional to the pulse energy.

5. Neutral Detection

Sensitive detection of neutral particles is essential for advancing matter-wave interferometry to biomolecules. This chapter reports on recent progress with superconducting nanowire detectors, which enable efficient detection of metastable atoms and neutral molecules.

In the previous chapters we discussed the launch and beam-splitting methods by which biomolecules shall be brought to interference. The last stage of an interferometer is the detection of the diffracted particles. For large biomolecules and clusters, detection poses a significant challenge, as these compounds are difficult to ionize at UV and VUV wavelengths in optical gratings [69, 71]. It may therefore be necessary to detect the neutral compounds directly. In the absence of electric charge, which is used in conventional secondary electron multipliers, detection must rely on the particles' kinetic energies. Consequently, secondary electron multipliers (SEM) are unsuited as detectors for matter-wave interferometry of large neutral molecules. While efficiencies depend on the mass and structure of the molecule, for proteins with kinetic energies $< 50\,\mathrm{eV}$, they can fall below $\eta \simeq 10^{-5}$ [89, 90]. Because the de Broglie wavelength λ_{dB} is inversely proportional to the momentum p, low kinetic energies are advantageous in matter-wave interferometry, as they correspond to longer wavelengths. There are, however, also practical experimental constraints. For example, in order to achieve a de Broglie wavelength greater than 100 fm for human insulin, which has a mass of $m \approx 5.8\,\mathrm{kDa}$ [45], a kinetic energy below $E = h^2/(2m\lambda_{\mathrm{dB}}^2) \approx 14\,\mathrm{eV}$ is required.

This chapter discusses superconducting cryogenic detectors, which have emerged as viable particle detection technologies in recent decades, with particular emphasis on superconducting nanowire detectors. An additional section addresses secondary electron emission detectors, a standard choice in many applications. These discussions provide the context for our recent publication [26], in which superconducting nanowire detectors were used to detect metastable atoms and neutral molecules with kinetic energies of a few electronvolts. We compared their efficiency to that of a traditional secondary electron multiplier. The experimental section details the setup, procedures, and findings in detail.

5.1. Superconducting detectors

5.1.1. Superconductivity

The superconducting state is a distinct thermodynamic phase characterized by two fundamental properties. First, it exhibits zero electrical resistance, allowing electrical currents to flow indefinitely without decrease. Second, a superconductor is a perfect diamagnet, expelling magnetic

fields from its interior in a phenomenon known as the Meissner effect [91]. A material enters the superconducting state only when the applied magnetic field, current density, and temperature are all below their respective critical values H_c, I_c, and T_c. For most superconductors, T_c lies in the single-digit Kelvin range, which is why the phenomenon was not observed until adequate cryogenic techniques became available [92].

A key concept in superconductivity is the dissipationless supercurrent density $I_s < I_c$. Unlike normal electrons, the superconducting charge carriers responsible for I_c do not experience mutual repulsion. A major step in modeling this non-Fermionic behavior was made by Ginzburg and Landau, who proposed that these charge carriers could be described by a single quasi-wavefunction, thereby behaving effectively as bosons. Contemporary understanding of superconductivity is based on the microscopic theory developed in 1957 by Bardeen, Cooper, and Schrieffer (BCS theory) [93]. BCS theory showed that electrons near the Fermi surface can form bound states, known as Cooper pairs, with a binding energy $E_g = 2\Delta \sim k_B T$. The pairing mechanism arises from a phonon-mediated attractive interaction between electrons, enabled by electronic screening in the medium. This interaction lowers the energy of a Cooper pair relative to two independent electrons at the Fermi surface with energy E_F, thereby stabilizing the bound state and overcoming the bare Coulomb repulsion. For temperatures $T < T_c$, Cooper pairs occupy a single quantum ground state, thus forming the basis for the quasi-wavefunction interpretation in Ginzburg–Landau theory. Phenomenologically, this follows from the Pauli exclusion principle, which requires the electrons within a Cooper pair to differ in either their momenta or spin orientation. Consequently, Cooper pairs exhibit bosonic behavior, allowing them to collectively occupy the superconducting ground state [91].

Upon absorption of energy $E > E_g = 2\Delta$, Cooper pairs dissociate into excited electrons, referred to as quasiparticles. These quasiparticles, also referred to as bogoliubons or bogolons, are described by fermionic ladder operators in BCS theory. They represent field-theoretic excitations of electron and hole states and therefore differ fundamentally from bare electrons [91]. Superconducting detectors exploit this transition from the superconducting to the excited state within the material by utilizing the generated quasiparticles or the local suppression of superconductivity to generate a measurable signal [92].

5.1.2. Types of superconducting detectors

In most superconductors, the energy gap Δ lies in the milli-electronvolt range. Consequently, absorption of a single photon with energy ranging from the deep ultraviolet to the long-wavelength infrared[4] can break hundreds to thousands of Cooper pairs [92]. The earliest optical superconducting detectors were developed for X-ray spectroscopy [95], and in recent decades their capability to detect and distinguish single photons has established them as standard instrumentation in optics laboratories.

[4] As an example, NbTiN possesses a critical temperature $T_c \approx 17\,\mathrm{K}$ [94]. At temperatures well below T_c, BCS theory predicts a superconducting gap of $2\Delta \approx 3.53\, k_B T_c \approx 5.2\,\mathrm{meV}$ [91]. Hence, breaking a single Cooper pair in NbTiN requires a photon with wavelength $\lambda = hc/2\Delta = 238\,\mu\mathrm{m}$. Irradiance in the optical range therefore generates thousands of quasiparticles per photon.

Superconducting Tunnel Junctions (STJs) and Kinetic Inductance Detectors (KIDs) both possess intrinsic photon-number-resolving capabilities. STJs operate via the Josephson effect, in which both Cooper pairs and quasiparticles can tunnel through an insulating barrier separating two superconductors. In a detector, this effect is utilized by applying a bias voltage across the junction. When an incident photon or particle generates excess quasiparticles, the resulting increase in tunneling current is measured. Because this current is proportional to the number of broken Cooper pairs, which in turn are proportional to the deposited energy, STJs are intrinsically energy-resolving. KIDs measure the change in inductance of a thin superconducting film resulting from the change in quasiparticle density following energy absorption. This inductance change is directly proportional to the deposited energy and is measured using a resonator [92].

A different approach is the Transition-Edge Sensor (TES), which operates as a calorimeter. In this case, detection is based on a change in heat associated with the superconducting phase transition following energy absorption. A thin superconducting film is voltage-biased at its transition temperature T_c and thermally coupled weakly to a heat sink. Within this narrow temperature range, energy deposition causes resistance variations that are read out through corresponding changes in Joule power dissipation [92].

5.1.3. Superconducting nanowire detectors

Principle of operation

Superconducting nanowire detectors (SNWDs), or superconduction single photon/particle detectors (SSPDs), combine the principles of thin superconducting films with the resistive response to energy absorption. They consist of a narrow superconducting strip of length l, with typical wire widths of $w = 50{-}500\,\mathrm{nm}$, and a thickness d of a few nanometers. The nanowires are typically patterned in a meander geometry to form pixels and to cover large active areas [92]. Figure 5.1 shows an image of the SSPD pixels used in the experimental section (5.3). In this configuration, the kinetic inductance of the wire is given by [96]:

$$L_K \propto \frac{l}{wd} \,. \tag{5.1}$$

Detection in nanowires relies on the local suppression of superconductivity following the absorption of sufficient energy. The wire is biased with an electrical current I_b below the critical value I_c. When energy is deposited into the material, it is locally distr 2ibuted, generating a cascade of quasiparticles that disrupt the supercurrent. This process ultimately results in the formation of a non-superconducting hotspot region [97]. Consequently, the bias supercurrent is forced to divert around the hotspot, increasing the local current density in proportion to the reduced superconducting cross-section of the wire. If this density reaches a critical threshold, whose exact value and physical origin remain under discussion [97], the entire cross-section of the wire becomes resistive with inductance L_K [96]. In operation, the nanowire is cooled well below its critical temperature T_c and biased with a current just below the critical current I_c. A bias current close to I_c increases the wire's sensitivity to hotspot formation [96]. Detection efficiency, however, does not necessarily scale monotonously with decreasing temperature. Instead, the optimal

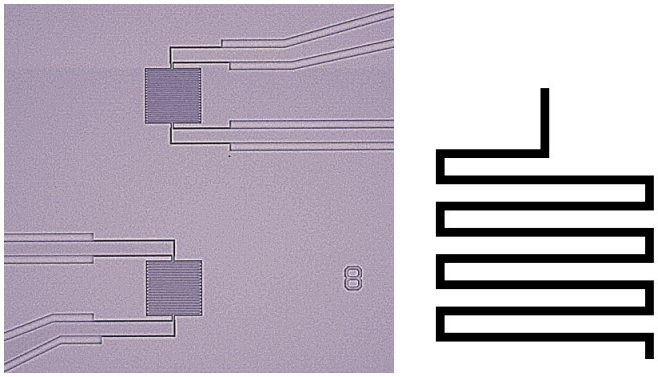

(a) (b)

Figure 5.1.: (a) Scanning electron microscopy image of the pixels of a superconducting nanowire single-photon detector (SSPD), showing their meander geometry. Adapted from [26]. (b) Schematic illustration of the meander geometry. Drawing is not to scale.

operating temperature depends on the photon energies to be detected, as different temperatures and corresponding bias currents can yield higher efficiency [97, 98]. This behavior may arise from variations in local thermal coupling within the wire [98]. To promote uniform hotspot formation across the active area, superconducting nanowires are typically fabricated from highly disordered materials [92].

Because superconductors are operated at temperatures of only a few Kelvin, ambient gases can freeze and condense onto the cooling stage and the detector surface. This effect, known as cushioning, must be avoided, as the growing layer can desorb upon particle impact and significantly reduce detection efficiency. For this reason, superconducting detectors are operated under ultra-high-vacuum conditions.

Hotspot & vortex models

An exact microscopic description of the detection mechanism in superconducting nanowires has not yet been established [97, 92]. The hotspot model, also referred to as the normal-core hotspot model, was the first theoretical framework proposed to explain the processes occurring within the wire. In this model, absorption of energy E is followed by a hotspot cascade, in which the resistive zone is assumed to have cylindrical symmetry and to expand radially from the hotspot center toward the nanowire edges [99]. The threshold bias current I_{th} required to initiate a detection is given by [100]:

$$I_{\mathrm{th}} = I_{\mathrm{c}}\left(1 - \gamma\frac{\sqrt{E}}{w}\right), \tag{5.2}$$

where w is the wire width and γ is a material- and geometry-dependent constant. Several extensions to this model have been proposed. When accounting for the diffusion of the quasiparticle cloud around the hotspot and its subsequent interaction with the supercurrent, some authors have

argued that the proportionality between bias current and energy should be linear rather than quadratic [99].

This deviation from the traditional expectation for the hotspot models, is due to the assumption that magnetic vortices may additionally play an important role in the suppression of superconductivity. The exact circumstances under which they form and when they are of relevance are also not agreed upon. Vortices may be produced in fluctuations following thermal activation in and around a cloud of non-equilibrium quasi-particles. One kind of fluctuation would be the depairing of a vortex-antivortex pair, which then traverse the strip. This deviation from the traditional expectation of hotspot models stems from the assumption that magnetic vortices may play an additional role in the suppression of superconductivity. The precise conditions for their formation and their relevance to detection events remain under debate. Vortices may arise from fluctuations following thermal activation in and around a cloud of non-equilibrium quasiparticles. One possible mechanism involves the depairing of a vortex-antivortex pair, after which the two vortices traverse the nanowire. Another involves a single vortex crossing the strip, thereby locally suppressing superconductivity [99, 97]. If the strip width exceeds approximately 4.4 times the Ginzburg-Landau coherence length, theory allows vortices to form. Owing to the small dimensions of the strips, they typically lie entirely within this length, permitting weak magnetic fields to penetrate the material [101]. Vortices have been proposed to account for the absence of spectral cut-offs in photon detection that would be expected in a theory based solely on hotspots. In particle detection, however, the exact microscopic processes are not of primary relevance, and the quadratic relationship in equation (5.2) has been found to agree well with experimental data [102].

Detector design & properties

Superconducting nanowires are typically patterned in a meander configuration to maximize the detection area covered by a single strip. The readout signal is obtained via a resistor connected in parallel to the nanowire. A schematic of the circuit is shown in figure 5.2. When the wire becomes resistive, the bias current is diverted into the readout circuit, where it is subsequently amplified. While the bias current is redirected, effects that could sustain the hotspot, such as Joule heating, are reduced in the nanowire, allowing it to cool below the critical temperature T_c and thereby reestablish superconductivity. This thermalization process occurs on a timescale of a few picoseconds [96]. Superconducting nanowires therefore intrinsically generate digital pulses, eliminating the need for external analog signal integration and readout. The absence of external readout electronics contributes to their exceptionally low noise levels, with dark count rates well below 1 Hz [92]. The detector dead time is determined almost entirely by the impedance of the wire, dominated by its inductance, and by the associated pulse decay time in the readout. It is typically on the order of nanoseconds. Both the rise time τ_r and the decay time τ_d of a voltage pulse are proportional to the wire inductance. Consequently, employing wires with a high ratio w/ld (see equation (5.1) yields the most effective strip detector [96].

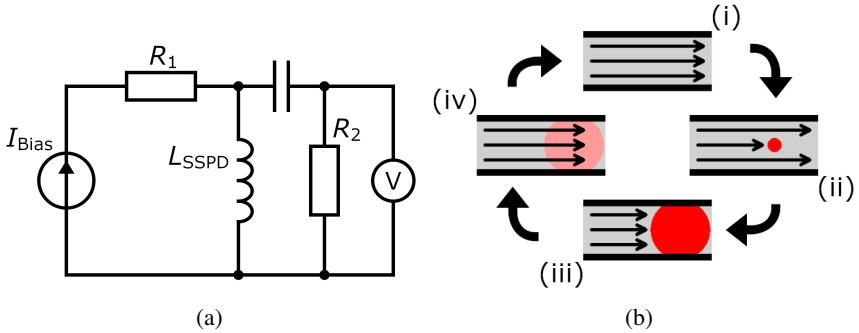

Figure 5.2.: (a) Circuit diagram of a SSPD readout. When the wire remains fully superconducting throughout its whole length, its inductance L_{SSPD} is effectively zero, so the bias current I_b is only impeded by the small resistance R_1. If superconductivity is suppressed locally, and L_{SSPD} reaches the threshold, where current flow through the resistance R_2 is favored, a diversion current arises and can be measured via a voltmeter connected in parallel to R_2. (b) shows the hotspot model of a superconducting wire. In (i) the supercurrent flows unhindered through the wire. Following energy absorption, a hotspot begins to form in (ii), which eventually grows large enough to block the whole flow as pictured in (iii). At this point the current is diverted to the readout. Shortly thereafter, thermalization cools the wire in (iv), allowing it to return to the fully superconducting state (i).

5.1.4. Superconducting nanorwires as particle detectors

The application of superconducting techniques to particle detection dates back to 1949, when superconducting bolometers were employed to detect α-particles in cosmic radiation [103]. Since the 1990s, superconducting cryogenic detectors, until then used primarily for photon detection, have also been applied as ion detectors in mass spectrometry, with early implementations predominantly employing superconducting tunnel junctions (STJs) for the detection of ions [104, 105, 106]. The first proof-of-principle demonstration of neutral-particle detection in 2009, when superconducting nanowires were used to detect biomolecules [107].

These tests reported detecting neutral molecules with masses ranging from 537 Da (β-carotene) to 66 kDa (bovine serum albumin), but questions remained open. Although it was ruled out that the noble gases used as seed gas contributed to the counts, it was not clear whether individual molecules were detected or clusters. Because both single molecules and molecule clusters implanted into the seeding beam are expected to reach the same velocity distribution, their respective kinetic energies differ drastically. The available evidence could not discern how strongly the signal depended on clusters, and whether single molecules were detected at all. Despite this uncertainty, neutral-molecule signal could be observed, thus demonstrating the applicability of superconducting materials for this purpose [107].

The study reported the detection of neutral molecules with masses ranging from 537 Da (β-carotene) to 66 kDa (bovine serum albumin), but several questions remained unresolved. Although

the noble gases used as seed gas were ruled out as a source of counts, it was unclear whether the detection events corresponded to individual molecules or to molecular clusters. Because both single molecules and clusters implanted into the seeding beam are expected to share the same velocity distribution, their kinetic energies differ substantially. The available experimental evidence could not determine to what extent the detected signal originated from clusters or whether single molecules had been successfully detected at all. Despite these uncertainties, the successful detection of neutral molecules was reported [107].

Recently, experiments conducted in our research group employed SSPD arrays as detectors in quadrupole mass spectrometry of insulin and vitamin B_{12} at kinetic energies ranging from 100 to 1000 eV. The results indicated an effective quantum yield of approximately 100% after accounting for the wire fill factor, exceeding the sensitivity of channel electron multipliers in this energy range by two to three orders of magnitude [102].

5.2. Channel electron multipliers

The core operating principle of a secondary, or channel electron multiplier (CEM) is that of a continuous dynode. When incident particles strike a material with sufficiently high kinetic energy, secondary electrons are emitted from the surface. In a CEM, the channel is a hollow, curved tube in which particles are detected by their collisions with the inner walls, initiating an electron cascade. The initial collision produces secondary electrons, which are immediately accelerated by a strong voltage gradient along the channel, typically on the order of a few kilovolts. These accelerated electrons strike the walls, releasing an additional δ free electrons per impact. This process initiates a charge cascade in which n successive multiplication events result in an overall gain $G = \delta^n$. The amplified charge is collected at the output and converted into a voltage pulse. Due to the background current inherent to a electronic readout, a discriminator is required to distinguish genuine particle impacts from noise [108]. Modern CEMs are fabricated from materials that optimize both secondary-emission characteristics and charge replenishment during operation. They are typically constructed from lead-glass matrices, which possess a high work function, thereby keeping thermal emission rates extremely low, and coated with emission-enhancing layers such as alkali, alkaline-earth, or semiconductor materials [109]. Optimal performance is achieved when primary particles impact the channel near its entrance, allowing the secondary-electron multiplication cascade to proceed over a longer path and thus reach higher gain, which is why single-channel detectors are often bent into a post-horn shape [109, 108].

5.2.1. Multichannel plates

A single channel multiplier functions as an individual pixel, as its signal readout only provides a positive output when a particle is detected. By arranging multiple CEMs in parallel, a two-dimensional array is formed, with each channel aperture serving as a discrete pixel. Such an array is referred to as a multichannel plate (MCP). The constituent channels are typically arranged in a hexagonal pattern to maximize the active area coverage per pixel. Curved channels are impractical in such an array and would increase the overall detector length. To address the

limitations of straight channels, a common approach is to employ two plates with channels tilted relative to one another, a configuration known as the Chevron arrangement. At tilt angles of approximately 15°, the change in trajectory is sufficient to prevent ions from propagating back to the channel output. By altering the electron trajectories, this design increases the probability of wall collisions, analogous to the effect of curved channels on secondary electrons. A single plate typically provides a gain of 10^3, while adding a second plate with its bias angle tilted relative to the first can yield gains exceeding 10^7 electrons per event at the readout. Furthermore, the absence of a straight path through the entire channel ensures that no incident particle can traverse the MCP without interacting [108, 109].

CEM detectors are particularly effective for charge detection, with quantum yields up to $\eta \simeq 90\%$ for single charged particles in the kinetic energy range of 1−3 keV [110]. In contrast, for neutral molecules with kinetic energies below 100 eV, the detection sensitivity can drop to $\eta \simeq 10^{-5}$ [26]. Hence, detection of larger macromolecules requires substantially higher impact energies. For species with masses exceeding 20 kDa, which covers over 80% of known proteins, impact energies greater than 40 keV are typically necessary to achieve reliable detection at CEMs [102]. Metastable atoms can be detected using CEMs, where the efficiency is determined by the secondary electron yield. Reported yields in the literature range from 10−70%, depending strongly on the surface material [79]. MCPs have already been utilized for the detection of diffracted metastable helium [111]. At the terminal velocities reached in supersonic expansion, both metastable helium ($m = 4$ Da) and argon ($m = 40$ Da) possess kinetic energies well below 1 eV [33]. Consequently, the detection signal originates entirely from the release of the atoms' internal excitation energy.

5.3. Detection of neutral atoms and molecules via their internal and kinetic energy

This section describes the experimental investigation of superconducting nanowire as detectors for particles, and especially neutral molecules. We evaluate their sensitivity to different forms of particle energy and to establish their potential as universal detectors for future matter-wave experiments, in comparison with traditional secondary electron multipliers.

5.3.1. Setup

The complete experimental setup is shown in figure 5.3. The experiment is conducted under vacuum, with two differential pumping stages separating the source chamber from the detection chamber. When the source is not active, the pressure in the detector chamber reaches the ultra-high-vacuum regime, with values as low as $p \sim 10^{-9}$ mbar. Such conditions are essential to minimize cushioning effects at the cryogenic detector. The distance between the source and the detector is $d = 125$ cm.

The setup can be divided into three main sections: the particle source, the differential pumping stages, and the detection chamber. The particle source generates atomic or molecular beams of

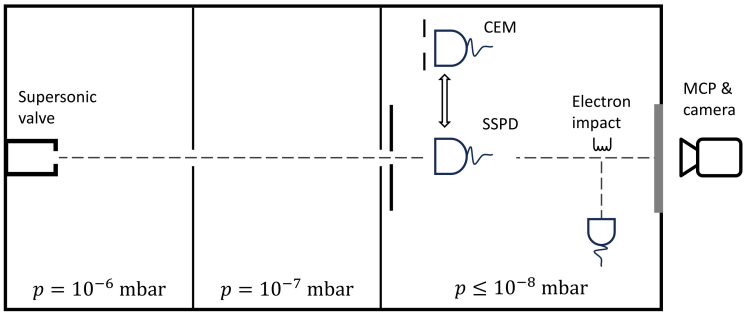

Figure 5.3.: Schematic of the complete experimental setup. An Even–Lavie valve produces particle beams, which pass through two differential pumping stages before entering the detection chamber. The detection chamber contains the cryogenic SSPD array and a channel electron multiplier (CEM), both mounted on translation stages for direct efficiency comparison. Additional diagnostics are provided by a quadrupole mass spectrometer and an MCP for beam profiling.

the desired species. These beams pass through the pumping stages, which reduce background pressure before the particles reach the detector. The following subsections describe each of these components in detail, beginning with the atomic and molecular beam source.

Atomic and molecular beam source

Experiments are conducted with three particle species: metastable helium (He^*), metastable argon (Ar^*), and perfluorodecalin (C10F18, $m = 462$ Da), which is seeded in helium. Perfluorodecalin is chemically inert and has a sufficiently high vapor pressure to self-seed in the Even–Lavie valve, enabling stable beam performance during the experiment. Consistent with other measurements of molecules seeded in helium, the particles are expected to remain in their electronic ground state, with integrated vibrational and rotational energy contents below 1 eV [26, 34]. Figure 5.4 shows the chemical structure of perfluorodecalin.

Two types of Even–Lavie valves are employed. One operates at room temperature and is equipped with a dielectric barrier discharge (DBD) to excite the gas atoms. The other is a heated source at $T = 200\,°C$, where helium serves as the carrier gas for perfluorodecalin. All experiments are performed with a valve pulse frequency of $f = 100$ Hz. For metastable atoms, the pulse length is set slightly above $\tau_{\text{pulse}} = 20\,\mu s$, whereas for perfluorodecalin it is $\tau_{\text{pulse}} = 11.5\,\mu s$. These pulse lengths can be set directly at the digital valve control. The difference in pulse lengths reflects ensures sufficient particle flux while avoiding excessive background gas load for the respective particle species and was determined experimentally, by selection a value that did not increase the source chamber pressure above $p = 10^{-5}$ mbar.

The valve pulse is triggered externally, while the pulse length is adjusted directly via the valve control. With the Even–Lavie's thermal terminal velocity given by $v_{\text{term}} \simeq \sqrt{5k_B T/m}$, based on equation (5.3), the expected velocities at $T = 300$ K for metastable helium and argon are $v_{\text{He}^*,\,\text{ex}}$

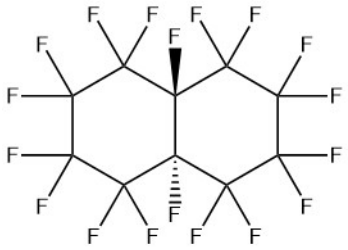

Figure 5.4.: Chemical structure of (trans-)perfluorodecalin.

and $v_{\mathrm{Ar}^*,\,\mathrm{ex}}$, respectively:

$$\begin{aligned} v_{\mathrm{He}^*,\mathrm{ex}} &= 1767\,\frac{\mathrm{m}}{\mathrm{s}}\,, \\ v_{\mathrm{Ar}^*,\mathrm{ex}} &= 558\,\frac{\mathrm{m}}{\mathrm{s}}\,. \end{aligned} \tag{5.3}$$

These theoretical estimates serve as a reference for later comparison with measured time-of-flight data, providing a consistency check on beam temperature and source performance.

Detector mounting

To enable direct comparison between the superconducting detector and the secondary electron emission detector, both are mounted on linear translation stages that allow precise positioning within the beam path during measurements. The SSPD is mounted vertically, while the CEM is mounted horizontally. This arrangement also makes it possible to characterize the beam profile by recording the count rate while scanning the detector position across the beam. All valves and detectors are synchronized by trigger pulses from a single pulse generator, ensuring precise timing between beam generation and detection.

Cryogenic detector

The superconducting detector, developed by Single Quantum, consists of an array of eight niobium titanium nitride (NbTiN) pixels sputtered on a 180 nm-thick SiO_2 layer. Each pixel is made of a single continuous nanowire arranged in a meander geometry, with wire widths ranging from 60 nm to 300 nm. Regardless of the wire width, each pixel covers an active area of $20\,\mu\mathrm{m} \times 20\,\mu\mathrm{m}$, corresponding to $400\,\mu\mathrm{m}^2$, with the same fill factor of 50%. The pixels are vertically separated by 50 µm, resulting in a total span of 510 µm from the upper edge of the first pixel to the lower edge of the last. The individual pixel specifications are summarized in Table 5.1.

The entire array is mounted on the cold stage of a pulse-tube cooler and operated at temperatures of $T \leq 3.8\,\mathrm{K}$. NbTiN superconductors typically have critical temperatures $T_\mathrm{c} > 10\,\mathrm{K}$, and their critical current density J_c reaches its maximum at around 4.8 K [94], allowing for a wide range of bias current settings. For all measurements, the bias current was adjusted such that the dark count rate of each pixel remained below 5 cps.

Table 5.1.: Specifications of the cryogenic detector used. Here w is the wire width, p the period of the wire meander, I_c the critical current, and I_b the bias current.

Pixel	1	2	2	4	5	6	7	8
w (nm)	60	70	85	100	150	200	250	300
p (nm)	120	140	170	200	300	400	500	600
I_c (µA)	5	5.8	8.9	10.5	19.7	22.9	36.0	34.9

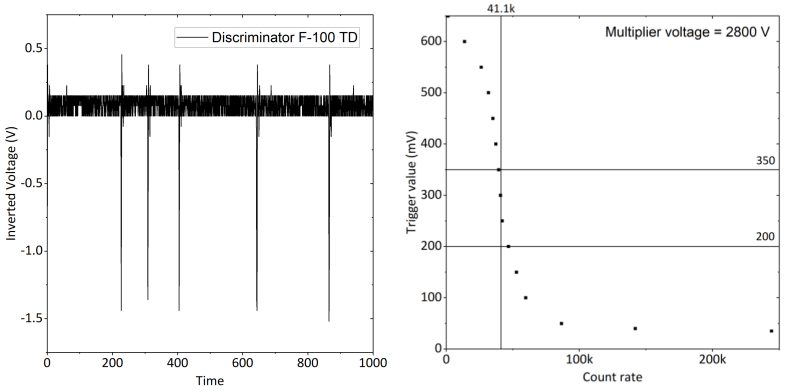

(a) (b)

Figure 5.5.: (a) CEM pulse shapes measured after the discriminator F-100TD. For a trigger value of 50 mV noise seems to be mostly suppressed, while signal pulses can be measured without interference form ringing. (b) Trigger voltage vs. dark count rate for an operating voltage of 2800 V at the CEM.

Channel electron multiplier

A single-channel electron multiplier (CEM) is mounted on a translation stage. The output signal is processed through an F-100TD discriminator (Advanced Research Instruments) and recorded digitally using a counter module from National Instruments. An aperture is installed directly in front of the channel entrance, with a width of 200 µm for helium and argon experiments and 2 mm for perfluorodecalin. The aperture makes it possible to scan the beam profile by moving the CEM stage while monitoring the signal, and it reduces the fraction of the beam reaching the channel entrance, thereby lowering count rates and preventing saturation in the readout. The spatial restriction also allows the effective beam cross section contributing to the signal to be determined if the beam profile is known.

Quadrupole mass spectrometer

To analyze the beam particles reaching the detector chamber, an Extrel electron-impact quadrupole mass spectrometer (EI-QMS) is positioned downstream of the array stage. When both the CEM and the SSPD array are retracted from the beam path, the beam enters the mass spectrometer

directly. This configuration enables verification of cluster formation in the beam and detection of unwanted particle species.

5.3.2. Experimental procedure

For each measurement, the experiment follows a fixed sequence to ensure reproducibility and consistent detector conditions. All valves and detectors are synchronized by a common pulse generator.

First, the Even–Lavie valve is triggered at the set repetition rate of $f = 100\,\mathrm{Hz}$, releasing a supersonic pulse of the selected particle species. For metastable species, the dielectric barrier discharge is activated simultaneously with the valve opening. In the case of perfluorodecalin, the heated source operates continuously at $T = 200\,^{\circ}\mathrm{C} = 473\,\mathrm{K}$ with helium as carrier gas.

Beam profiles are measured by scanning the appropriate detector stage across the beam and recording the count rate at each position. For quantum efficiency comparisons, measurements are taken alternately with the SSPD array and the CEM in the beam path, using identical source settings. The MCP and quadrupole mass spectrometer are employed either for beam diagnostics before measurements or for verifying cluster-free operation during parameter changes.

For each measurement, data are collected for a duration sufficient to ensure adequate statistical accuracy.

Table 5.2.: Overview of particle source parameters. All measurements were performed with a pulse frequency of $f = 100\,\mathrm{Hz}$. Here, p_0 is the backing pressure at the valve, τ_{pulse} the valve pulse length, and T the source temperature.

Particle	Valve type	T (K)	p_0 (bar)	τ_{pulse} (ms)
He^*	Cold, DBD	≈ 293	10	22.0
Ar^*	Cold, DBD	≈ 293	4	22.0
$C_{10}F_{18}$	Heated, He-seeded	473	20, 30, 40, 50	11.5

5.3.3. Preliminary checks

Light signal at detectors

When operating the superconducting detector array, all sources of ambient light must be blocked from the detector chamber, as stray photons can produce counting events. For the 60 nm wire, daylight exposure during experimental work resulted in count rates in the kilohertz range. In addition, plasma formation during the dielectric barrier discharge in the Even–Lavie valve emits photons with each pulse. To suppress signals from these photons, each pixel readout is routed through an RF switch that blocks output for the first 130 ms following the valve trigger. The fastest atoms in the experiment are metastable helium, with a median velocity of approximately $v_{\mathrm{He}^*,\mathrm{ex}} \approx 1650\,\mathrm{m/s}$. During the 130 ms blocking interval, these atoms travel a distance of $s = 1650\,\mathrm{m/s} \times 130\,\mathrm{ms} = 0.2145\,\mathrm{m}$, which is considerably shorter than the 1.25 m

separation between the source and the detector, thus ensuring that only photon-induced events are suppressed.

For the channel electron multiplier, the digital readout is performed using a counter module from National Instruments, which receives its input from the discriminator described in the following paragraph. As with the superconducting detector, counts occurring within 130 ms after a valve pulse are suppressed.

CEM operating voltage and readout

Optimizing the CEM performance relies on the interplay between the operating voltage and the trigger threshold at the readout. The operating voltage controls the gain of the multiplier, thereby determining the amplitude of the output voltage pulses. The trigger threshold then defines the minimum pulse amplitude required for an event to be registered.

In the setup, the CEM output is processed through an F-100TD discriminator, which substantially improves the signal-to-noise ratio at the readout. Ideally, all output pulses would exhibit a Gaussian-like shape with uniform amplitude. In practice, however, perturbations introduced during the electron multiplication process, as well as subsequent electronic noise, produce pulses with differing shapes and amplitudes. Another issue is signal ringing, which occurs when a single pulse induces multiple oscillations exceeding the discriminator threshold. If these oscillations are sufficiently separated in time, may be erroneously registered as multiple events, leading to potentially significant overcounting. In our configuration, the F-100TD discriminator achieved a sufficiently high signal-to-noise ratio to assume negligible contribution from ringing. Figure 5.5(a) shows a measurement of dark counts acquired with the discriminator in place. To optimize the operating voltages, the procedure recommended by Advanced Research Instruments in the F-100TD manual was followed. The first step is to ensure that the discriminator suppresses electronic noise. This is verified by confirming that the dark count rate can be reduced below 10 cps with all signal sources, including light, blocked. Next, the beam source is activated, and the trigger voltage is varied. The optimal setting lies within a region where small voltage changes produce minimal variation in count rate. Figure 5.5(b) shows a representative curve obtained during the experimental measurements.

A CEM operating voltage of 2800 V and a discriminator trigger voltage of 275 mV were found to be well suited for the present setup. The count rates shown in figure 5.5(b) were recorded using an oscilloscope rather than the NI counter, as the latter was unable to reliably process signals above 100 kHz. At such high rates, the oscilloscope registers up to twice as many counts. However, in the range used for the actual measurements, the two devices yielded comparable count rates.

Beam profile

Accurate knowledge of the beam profile is essential for comparing detector signal rates. In the setup, the SSPD array and the CEM are mounted on orthogonal linear stages, so each probes only

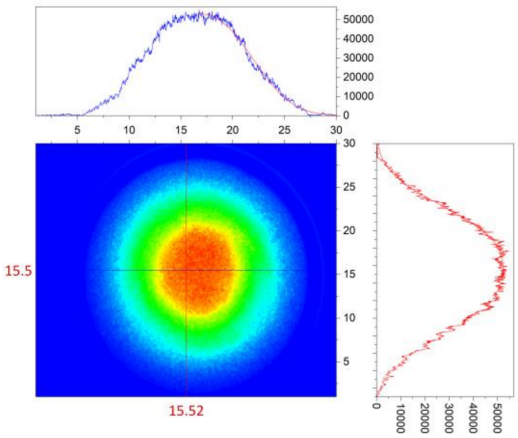

Figure 5.6.: Beam profile of a He^* beam at 2 m distance to the source. Its diameter is $\simeq 9.7$ mm. Plot values are arbitrary.

a cross-section of the beam. Prior to the main experiments, the beam from the DBD-assisted Even–Lavie valve was characterized with a Photonis Advanced Performance Long-Life MCP, mounted on a flange at the end of the detector chamber at a distance of $d_{\mathrm{MCP}} = (241 \pm 3)$ cm. The MCP was read out optically via a phosphor screen. For metastable helium, the profile, shown in figure 5.6, is approximately circular, with a flat-top super-Gaussian central region of about 5 mm in width. Eeach SSPD pixel has a width of 20 µm, and the full array spans 510 µm vertically. The largest aperture used with the CEM is 2 mm. Consequently, the SSPD effectively measures a flat-top portion of the beam, whereas along the vertical axis, the CEM response is given by the convolution of a flat-top profile of ~ 5 mm width with the corresponding aperture slit in front of the channel entrance.

Relative quantum detection efficiency

To determine the relative quantum detection efficiency η^*_{rel} between the detector types, the measured count rates are normalized to the respective active detection areas. Each SSPD pixel has an active area of 400 µm^2, fully contained within the beam cross-section. In contrast, the aperture in front of the single-channel electron multiplier is sufficiently large to encompass the entire beam profile downstream of the aperture. Using the measured beam profile, the effective beam area incident on the CEM can be inferred, enabling a direct comparison of detection efficiencies.

Cluster formation

Additional measures were implemented to suppress cluster formation, as n-fold clusters travel at nearly the same velocity as monomers, corresponding to a n-fold higher kinetic energy. This effect can raise the detection threshold substantially and, for perfluorodecalin, would compromise sensitivity to low-energy particles. Cluster suppression is thus essential to ensure detection of

particles with kinetic energies in the low-eV range.

Cluster formation depends strongly on nozzle conditions such as temperature, backing pressure, and gas density [112]. With this background, keeping pressures and valve opening times low was the primary strategy for suppressing clustering. Clustering was monitored via electron-impact quadrupole mass spectrometry (EI-QMS), where n-clusters appear at integer multiples of the monomer m/z. While no helium clusters were observed, argon required additional analysis near the cluster threshold. In this case, counts above the monomer m/z were summed and plotted against the nominal valve opening time τ_{nom}. At $\tau_{\mathrm{nom}} = 22\,\mu\mathrm{s}$ and varying backing pressure, a sharp increase appeared for $p > 8\,\mathrm{bar}$ (figure 5.7a). Consistent with scaling laws introduced by Hagena [113], all argon experiments were conducted at $p = 4\,\mathrm{bar}$, below the onset pressure.

For perfluorodecalin, seeded in helium at $p = 50\,\mathrm{bar}$ and $T_0 = 200\,\mathrm{K}$, τ_{nom} was varied from 11.5 µs to 14.5 µs in 0.1–0.5 µs steps. Clustering onset occurred at different τ_{nom} values depending on the sample loading volume. With minimal loading, it began at $\tau_{\mathrm{nom}} > 13.5\,\mu\mathrm{s}$ (figure 5.7b). All perfluorodecalin measurements were therefore performed at $\tau_{\mathrm{nom}} = 11.5\,\mu\mathrm{s}$ to ensure cluster-free conditions.

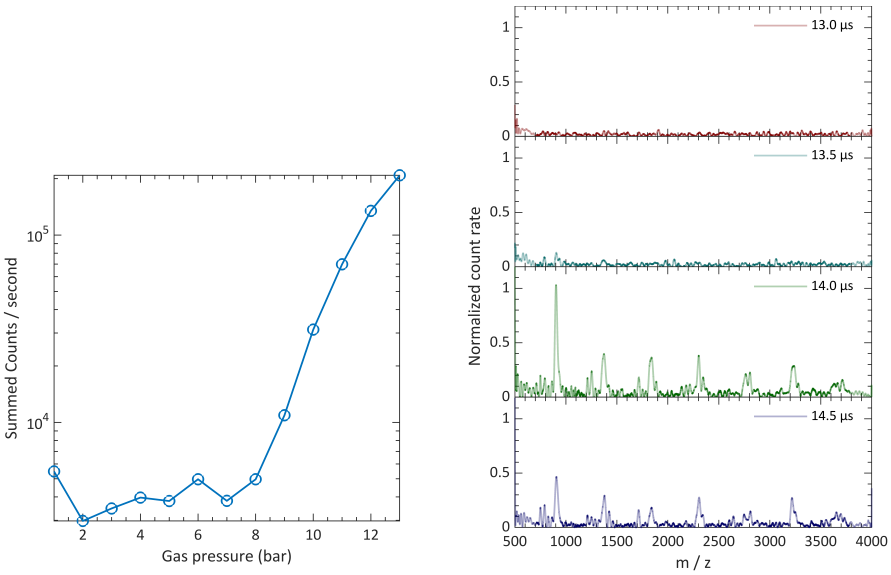

(a) (b)

Figure 5.7.: (a) Summed up QMS signal count rates between between 600 Da/e and 2000 Da/e while operating an Ar*-beam. (b) m/z spectra of perfluorodecalin for different nominal valve opening times τ_{nom}. The onset of clustering between $\tau_{\mathrm{nom}} = 13.5\,\mu\mathrm{s}$ and $\tau_{\mathrm{nom}} = 14.0\,\mu\mathrm{s}$ is clearly visible.

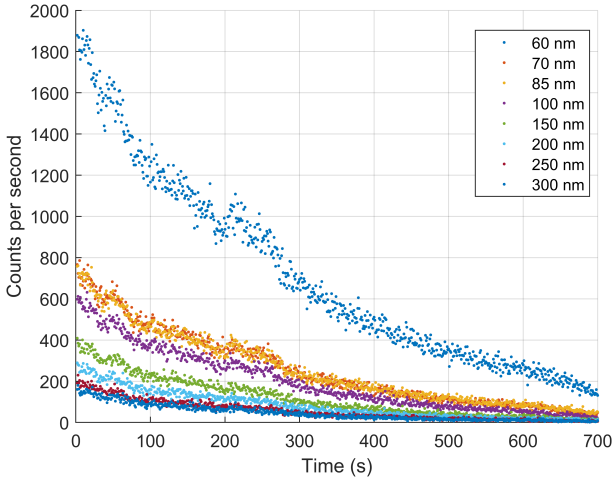

Figure 5.8.: Signal degradation over time for perfluorodecalin when the source is overloaded. The effect is attributed to cushioning and can be reversed by warming the system to room temperature.

Monolayer deposition

During initial measurements with metastable argon and perfluorodecalin, pronounced cushioning was observed, manifested as a rapid signal decrease over short measurement times, as shown in figure 5.8. No such effect was detected for metastable helium. For argon, nitrogen, and other background gas species, heating the detector surface to 30 K was sufficient to remove the frozen layer. Perfluorodecalin required substantially higher temperatures due to its higher melting point. In both cases, the effect was eliminated after adjusting the clustering threshold parameters described above. For perfluorodecalin, it was also essential to minimize the sample loading volume, as excessive loading appeared to promote cluster formation, which we attributed to the entrainment of small liquid droplets during the supersonic expansion.

5.3.4. Results

Beam profile

With metastable helium, the measured beam profile yielded a horizontal radius of $r_\mathrm{h} = 2.80\,\mathrm{mm}$ and a vertical radius of $r_v = (2.36 \pm 0.03)\,\mathrm{mm}$. The radii were obtained by fitting the measured profiles with a super-Gaussian function:

$$f(x) = A \exp\left(- \left(\frac{x - x_\mathrm{c}}{B} \right)^n \right), \tag{5.4}$$

where the fitted parameter B corresponds to the beam radius in the respective direction.

The horizontal radius was determined from a single CEM scan, shown in figure 5.9(a), while the vertical radius is the mean from scans with all eight SSPD pixels, shown in figure 5.9(b), which

also provides the statistical uncertainty. The resulting profile is elliptical, with an aspect ratio of 0.843 (vertical/horizontal), giving a total beam cross-sectional area of:

$$A = \pi \cdot 2.80\,\text{mm} \cdot 2.36\,\text{mm} = 20.76\,\text{mm}^2\,, \tag{5.5}$$

representing the full signal area accessible to the CEM.

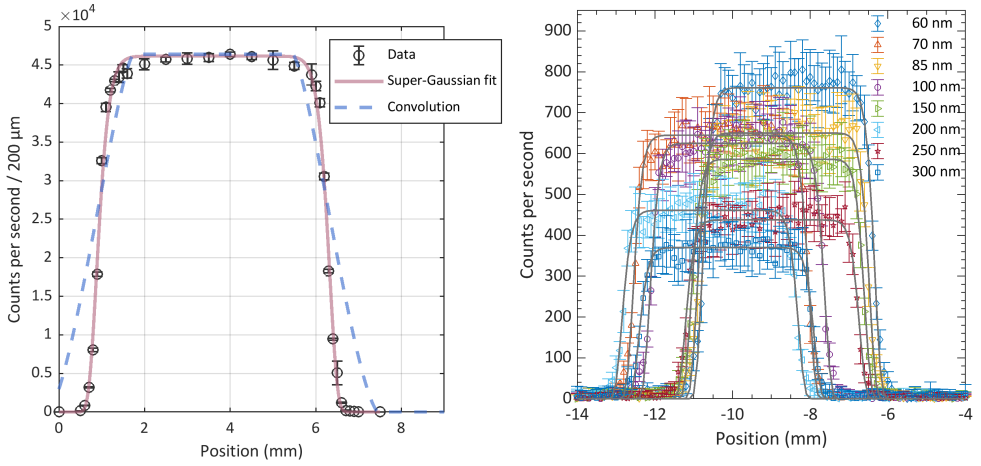

(a) (b)

Figure 5.9.: Beam profile measurements with He*. (a) Signal rates measured with the CEM for different central positions of the 200 µm slit, together with a super-Gaussian fit (solid line) and the convolution of a 5 mm circular aperture with the slit (dashed line). (b) Vertical beam profiles recorded with each SSPD pixel, each individually fitted with a super-Gaussian.

Time of flight

For metastable helium and argon, TOF spectra were measured with the SSPD array. Figure 5.10(a) shows the spectra for both species at the 60 nm wire. Each spectrum was fitted with a Maxwell–Boltzmann distribution, yielding mean velocities of:

$$\begin{aligned} v_{\text{He}^*} &= (1660 \pm 707)\,\frac{\text{m}}{\text{s}}\,, \\ v_{\text{Ar}^*} &= (610 \pm 60)\,\frac{\text{m}}{\text{s}}\,. \end{aligned} \tag{5.6}$$

The uncertainties are the standard deviations of the fitted peak positions. Their corresponding velocity spreads, given by the FWHM of the fits, are:

$$\begin{aligned} \Delta v_{\text{He}^*} &= 158\,\frac{\text{m}}{\text{s}}\,, \\ \Delta v_{\text{Ar}^*} &= 150\,\frac{\text{m}}{\text{s}}\,. \end{aligned} \tag{5.7}$$

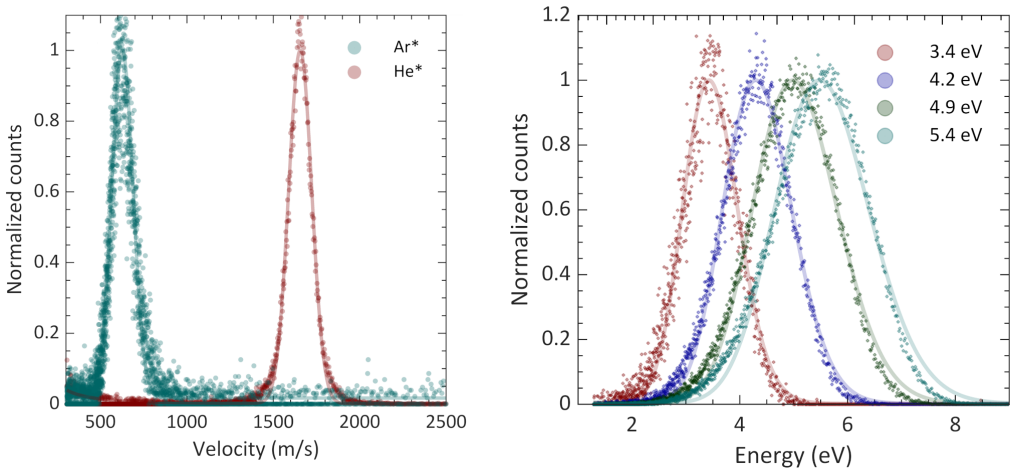

(a) (b)

Figure 5.10.: Results of the time-of-flight measurements for different particle species at the 60 nm wire. (a) shows the spectra of metastable helium (He^*) and argon (Ar^*). (b) shows the spectra of perfluorodecalin seeded in different background pressures, which results in different velocities and therefore kinetic energies.

Measured kinetic energies of neutral perfluorodecalin

For perfluorodecalin, TOF spectra were recorded at helium backing pressures of 20 bar, 30 bar, 40 bar, and 50 bar. Figure 5.10(b) shows the spectra with velocities converted to kinetic energy, each fitted with a Maxwell–Boltzmann distribution. The peak kinetic energies from the fits are:

$$\begin{aligned} E_{20\,\mathrm{bar}} &= (3.45 \pm 0.52)\,\mathrm{eV}\,, \\ E_{30\,\mathrm{bar}} &= (4.33 \pm 0.65)\,\mathrm{eV}\,, \\ E_{40\,\mathrm{bar}} &= (5.00 \pm 0.80)\,\mathrm{eV}\,, \\ E_{50\,\mathrm{bar}} &= (5.77 \pm 0.94)\,\mathrm{eV}\,, \end{aligned} \tag{5.8}$$

with uncertainties corresponding to the standard deviation at the peak. The FWHM values of the fitted curves are:

$$\begin{aligned} \Delta E_{20\,\mathrm{bar}} &= 1.23\,\mathrm{eV}\,, \\ \Delta E_{30\,\mathrm{bar}} &= 1.54\,\mathrm{eV}\,, \\ \Delta E_{40\,\mathrm{bar}} &= 1.90\,\mathrm{eV}\,, \\ \Delta E_{50\,\mathrm{bar}} &= 2.22\,\mathrm{eV}\,. \end{aligned} \tag{5.9}$$

Relative quantum detection efficiency

Both the CEM and the SSPD detected the tested metastable atoms. After normalizing the count rates to the active detector areas, the relative efficiency $\eta^*\mathrm{rel}$ can be compared. Figure 5.11 shows $\eta^*\mathrm{rel}$

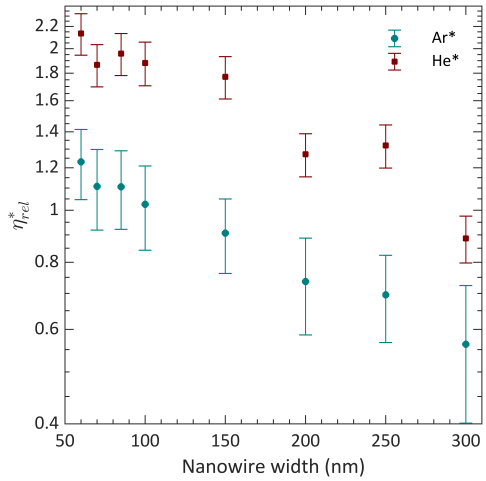

Figure 5.11.: Relative quantum detection efficiencies between SSPD and CEM detectors. The error bars represent the statistical uncertainty of the measurements.

for the eight SSPD pixels for He* and Ar*, with the SSPD signal corrected for its 50% fill factor. The uncertainties arise from temporal instabilities in the CEM signal during the measurements. The count rate correspond to a count rate for He* of $\approx$ per $-$ mode = symbol1014 sr^{-1} s, which is on the order of signal that is expected at the center of the beam profile [37]. We thus approximate an absolute quantum detection efficiency of ~ 1 for the thin wires.

For He*, the SSPD outperforms the CEM at every pixel except the one with the widest nanowire width of 300 nm, which still achieves nearly the same efficiency. For widths up to 150 nm, SSPD detection of metastable argon also exceeds that of the CEM. Across all pixels, the SSPD's relative efficiency η^*rel is almost twice as high for He* as for Ar*.

Bias current scans

Figure 5.12(a) shows bias current scans for the 60 nm wire with He* and Ar*. For He*, the $I_\mathrm{b}/I_\mathrm{c}$ offset, its relative value at maximum count rate, is approximately 10% lower than for Ar*. The same trend is observed for perfluorodecalin, as shown in figure 5.12(b) for the different kinetic energies. Lower kinetic energies consistently shift the maximum count rate to lower $I_\mathrm{b}/I_\mathrm{c}$ ratios.

Cutoff energies

The relative detection efficiencies of the SSPD pixels, which consistently yielded the highest count rate, are shown in figure 5.13(a). At the lowest kinetic energy, $E_{20\,\mathrm{bar}} = 3.45$ eV, the 300 nm wire registered nearly two orders of magnitude fewer counts than the 60 nm wire. The relative efficiency rises approximately exponentially with deposited energy, until detection rates reach

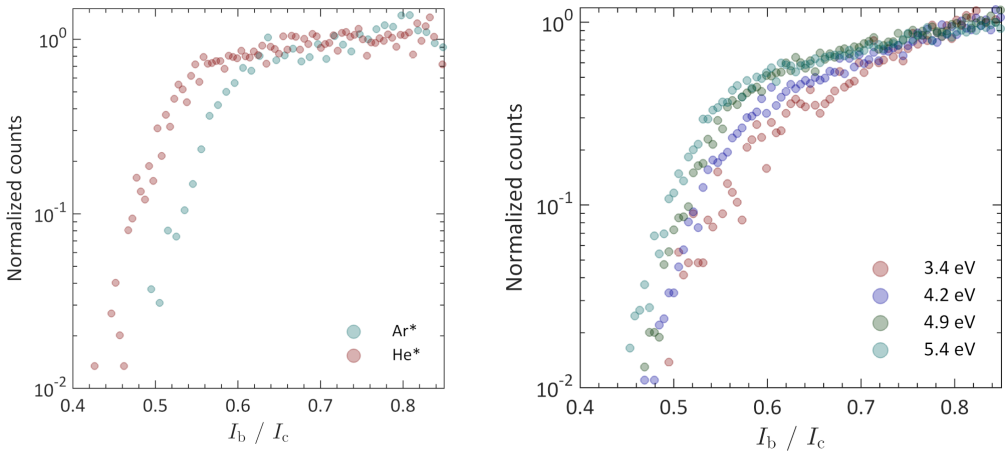

Figure 5.12.: Results of bias current scans for the 60 nm wire. (a) Scans for metastable helium (He*) and argon (Ar*). (b) Scans for perfluorodecalin seeded in helium at different backing pressures, corresponding to different kinetic energies.

parity.

A closer analysis of this exponential trend reveals distinct cutoff energies for each pixel, which are defined as the energy at which the relative efficiency $\eta_{\mathrm{rel},1}$ reaches unity in the logarithmic plots of figure 5.13(a). Figure 5.13(b) shows the extrapolated energies at which different pixels are expected to reach the same signal detection rate and thereby the same efficiency as pixel 1. They follow an approximately linear scaling with nanowire width, such that a wire twice as wide as another has roughly twice the cutoff energy.

5.3.5. Discussion

The SSPD as particle detector

For metastable atoms, the measured detection efficiencies are in good agreement with the literature value of approximately unity, confirming that the SSPD detects He* with near-perfect quantum yield. The relative efficiencies between He* and Ar* closely follow the ratio of their internal energies, demonstrating the nanowire detector's intrinsic energy-resolving capability, with response proportional to the available excitation energy. Since the kinetic energy of the metastable atoms lies far below the detection threshold, the signal can be attributed entirely to internal energy deposition.

For neutral perfluorodecalin molecules, detection was achieved down to kinetic energies of 3.45 eV, and potentially as low as 2.8 eV when considering the extrapolated onset. As these molecules were seeded in helium and detected without prior ionization, this constitutes unambiguous detection of neutral, ground-state molecules at very low energies. The lower bound found here is significantly

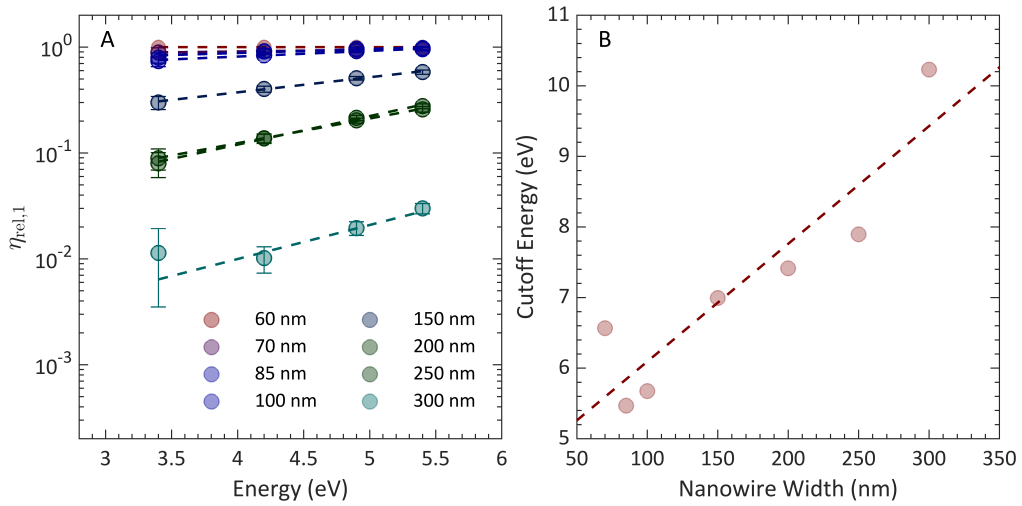

Figure 5.13.: (a) Relative detection efficiency $\eta_{\mathrm{rel},1}$ for each pixel, normalized to the count rate of the 60 nm pixel (thinnest wire). The fitted curves indicate an exponential dependence of $\eta_{\mathrm{rel},1}$ on deposited energy. (b) Corresponding cutoff energies, defined as the energies at which the fits in (a) reach unity, i.e., where the pixel's efficiency matches that of the 60 nm pixel. A linear fit to these cutoff values is also shown.

below the detection thresholds of conventional channel electron multipliers, highlighting the unique capability of SSPDs to detect low-energy neutral particles.

In addition to high quantum yield, the SSPD array offers several experimental advantages. Bias current scans confirm that the device can resolve differences in deposited energy, providing intrinsic energy discrimination without modification of the optical or electronic readout. The pixel size enables sub-millimeter spatial resolution in the beam profile, while the nanosecond-scale timing resolution supports precise time-of-flight measurements. Together, these capabilities establish the SSPD as a versatile, energy-sensitive detector for neutral atoms and molecules.

Future prospects for biomolecule interferometry

The combination of high efficiency, low detection thresholds, and fine spatial and temporal resolution opens promising prospects for matter-wave interferometry with complex particles. Insulin molecules with kinetic energies in the 2–3 eV range are well within the demonstrated detection capabilities, and the inferred threshold suggests that even kinetic energies around 1 eV may be detectable, potentially bringing large proteins such as hemoglobin within reach. This capability marks an important step toward extending high-mass interferometry to heavier and slower particles, where traditional ionization-based detectors are ineffective.

Various interferometric techniques could benefit substantially from the ability to detect neutral

atoms and molecules with kinetic energies in the low-eV range, including applications in structure analysis [114, 115] and surface analysis [116, 117]. Such methods employ diffraction at the material lattice, but require energies of ~ 1 keV the direction parallel to the surface, to allow for efficient detection. The ability to detect neutral particles at much lower impact energies would permit the use of atoms with less destructive potential for the probed material and increase the accessible de Broglie wavelengths.

The combination of high efficiency, low detection thresholds, and fine spatial and temporal resolution opens promising prospects for matter-wave interferometry with complex particles. Insulin molecules with kinetic energies in the 2–3 eV range are already within demonstrated detection capabilities, and the inferred threshold suggests that even energies around 1 eV may be detectable, potentially bringing large proteins such as hemoglobin within reach. This capability marks an important step toward extending high-mass interferometry to heavier and slower particles, where traditional ionization-based detectors are ineffective.

Various interferometric techniques could benefit from the ability to detect neutral atoms and molecules at low impact energies could transform methods in structure and surface analysis [114, 115, 116, 117]. Whereas conventional approaches require keV-energies parallel to the surface to achieve sufficient detection efficiency, low-eV sensitivity would enable the use of far gentler projectiles, increasing the accessible de Broglie wavelengths while reducing damage to the probed material.

The methods discussed in this thesis provide the essential ingredients for extending matter-wave interferometry to biomolecules: bright and coherent beams, absorptive beam splitters based on photocleavage, and detectors capable of registering neutral particles at kinetic energies down to the few-eV range. With these tools, interferometric studies can continue to advance toward increasingly complex biomolecules. Diffraction of molecules as complex as insulin or hemoglobin would mark a decisive milestone, uniting a stringent test of quantum mechanics at macroscopic scales with new opportunities for quantum-enhanced sensing and structural studies of the fundamental building blocks of life.

Bibliography

[1] L. de Broglie. Waves and quanta. *Nature*, 112(2815):540–540, October 1923.

[2] A. H. Compton. A quantum theory of the scattering of x-rays by light elements. *Phys. Rev.*, 21(5):483–502, May 1923.

[3] L. de Broglie. Recherches sur la théorie des quanta. *Ann. de Phys.*, 3:22–128, 1925. English translation available at `https://fondationlouisdebroglie.org/LDB-oeuvres/De_Broglie_Kracklauer.pdf`.

[4] E. Schrödinger. An undulatory theory of the mechanics of atoms and molecules. *Phys. Rev.*, 28(6):1049–1070, December 1926.

[5] P.A.M. Dirac. The quantum theory of the electron. *Proc. R. Soc. Lond.*, 117(778):610–624, February 1928.

[6] C. Davisson and L. H. Germer. Diffraction of electrons by a crystal of nickel. *Phys. Rev.*, 30(6):705–740, December 1927.

[7] I. Estermann and O. Stern. Beugung von molekularstrahlen. *Z. Phys.*, 61(1–2):95–125, January 1930.

[8] D. P. Mitchell and P. N. Powers. Bragg reflection of slow neutrons. *Phys. Rev.*, 50(5):486–487, September 1936.

[9] H. Halban and P. Preiswerk. Preuve expérimentale de la diffraction des neutrons. *C. R. Acad. Sci. Paris*, 203:73–75, 1936.

[10] E. O. Wollan and L. B. Borst. Physics section iii monthly report for the period ending december 31, 1944. *Report No.: M-CP-2222, Clinton Laboratories, Oak Ridge, TN, USA*, 1945.

[11] P. E. Moskowitz, P. L. Gould, S. R. Atlas, and D. E. Pritchard. Diffraction of an atomic beam by standing-wave radiation. *Phys. Rev. Lett.*, 51(5):370–373, August 1983.

[12] P. J. Martin, P. L. Gould, B. G. Oldaker, A. H. Miklich, and D. E. Pritchard. Diffraction of atoms moving through a standing light wave. *Phys. Rev. A*, 36(5):2495–2498, September 1987.

[13] D. W. Keith, M. L. Schattenburg, H. I. Smith, and D. E. Pritchard. Diffraction of atoms by a transmission grating. *Phys. Rev. Lett.*, 61(14):1580–1583, October 1988.

[14] Ch.J. Bordé. Atomic interferometry with internal state labelling. *Phys. Lett. A*, 140(1–2):10–12, September 1989.

[15] F. Riehle, Th. Kisters, A. Witte, J. Helmcke, and Ch. J. Bordé. Optical ramsey spectroscopy in a rotating frame: Sagnac effect in a matter-wave interferometer. *Phys. Rev. Lett.*, 67(2):177–180, July 1991.

[16] M. Kasevich and S. Chu. Atomic interferometry using stimulated raman transitions. *Phys. Rev. Lett.*, 67(2):181–184, July 1991.

[17] K. B. Davis, M. O. Mewes, M. R. Andrews, N. J. van Druten, D. S. Durfee, D. M. Kurn, and W. Ketterle. Bose-einstein condensation in a gas of sodium atoms. *Phys. Rev. Lett.*, 75(22):3969–3973, November 1995.

[18] K. Huang. *Statistical mechanics*. Wiley, New York, NY [u.a.], 2. ed. edition, 1987.

[19] Ch.J. Bordé, N. Courtier, F. du Burck, A.N. Goncharov, and M. Gorlicki. Molecular interferometry experiments. *Phys. Lett. A*, 188(3):187–197, May 1994.

[20] M. Arndt, O. Nairz, J. Vos-Andreae, C. Keller, G. van der Zouw, and A. Zeilinger. Wave–particle duality of c60 molecules. *Nature*, 401(6754):680–682, October 1999.

[21] Y. Y. Fein, P. Geyer, P. Zwick, F. Kiałka, S. Pedalino, M. Mayor, S. Gerlich, and M. Arndt. Quantum superposition of molecules beyond 25 kda. *Nat. Phys.*, 15(12):1242–1245, September 2019.

[22] A. Shayeghi, P. Rieser, G. Richter, U. Sezer, J. H. Rodewald, P. Geyer, T. J. Martinez, and M. Arndt. Matter-wave interference of a native polypeptide. *Nat. Commun.*, 11(1), March 2020.

[23] L. Mairhofer, S. Eibenberger, J. P. Cotter, M. Romirer, A. Shayeghi, and M. Arndt. Quantum-assisted metrology of neutral vitamins in the gas phase. *Angew. Chem. Int. Ed.*, 56(36):10947–10951, July 2017.

[24] J. Schätti, V. Köhler, M. Mayor, Y. Y. Fein, P. Geyer, L. Mairhofer, S. Gerlich, and M. Arndt. Matter–wave interference and deflection of tripeptides decorated with fluorinated alkyl chains. *J. Mass Spectrom.*, 55(6), May 2020.

[25] N. Dörre, J. Rodewald, P. Geyer, B. von Issendorff, P. Haslinger, and M. Arndt. Photofragmentation beam splitters for matter-wave interferometry. *Phys. Rev. Lett.*, 113(23):233001, December 2014.

[26] M. Strauß, R. Gourgues, M. F. X. Mauser, L. Kulman, M. Castaneda, A. Fognini, A. Shayeghi, P. Geyer, and M. Arndt. Superconducting nanowire detection of neutral atoms and molecules via their internal and kinetic energy in the ev range. *Adv. Phys. Res.*, 4(2), December 2024.

[27] S. Eibenberger, S. Gerlich, M. Arndt, M. Mayor, and J. Tüxen. Matter–wave interference of particles selected from a molecular library with masses exceeding 10000 amu. *Phys. Chem. Chem. Phys.*, 15(35):14696, 2013.

[28] M. Arndt, N. Dörre, S. Eibenberger, P. Haslinger, J. Rodewald, K. Hornberger, S. Nimmrichter, and M. Mayor. Matter wave interferometry with composite quantum objects. *Proceedings of the International School of Physics "Enrico Fermi"*, 188:89–141, 2014.

[29] Y. Segev, N. Bibelnik, N. Akerman, Y. Shagam, A. Luski, M. Karpov, J. Narevicius, and E. Narevicius. Molecular beam brightening by shock-wave suppression. *Sci. Adv.*, 3(3), March 2017.

[30] N. Ramsey. *Molecular Beams*. Oxford University Press, January 1986.

[31] R. Campargue. Progress in overexpanded supersonic jets and skimmed molecular beams in free-jet zones of silence. *J. Phys. Chem.*, 88(20):4466–4474, September 1984.

[32] R. Cattolica, F. Robben, L. Talbot, and D. R. Willis. Translational nonequilibrium in free jet expansions. *Phys. Fluids*, 17(10):1793–1807, October 1974.

[33] U. Even. "the even-lavie valve as a source for high intensity supersonic beam". *EPJ Tech. Instrum.*, 2(1), December 2015.

[34] U. Even, J. Jortner, D. Noy, N. Lavie, and C. Cossart-Magos. Cooling of large molecules below 1 k and he clusters formation. *J. Chem. Phys.*, 112(18):8068–8071, May 2000.

[35] M. Belan, S. De Ponte, and D. Tordella. Highly underexpanded jets in the presence of a density jump between an ambient gas and a jet. *Phys. Rev. E*, 82(2):026303, August 2010.

[36] W. Christen. Stationary flow conditions in pulsed supersonic beams. *J. Chem. Phys.*, 139(15), October 2013.

[37] K. Luria, N. Lavie, and U. Even. Dielectric barrier discharge source for supersonic beams. *Rev. Sci. Instrum.*, 80(10), October 2009.

[38] W. Jin, H. Bromberger, L. He, M. Johny, I. S. Vinklárek, K. Długołęcki, A. Samartsev, F. Calegari, S. Trippel, and J. Küpper. A versatile and transportable endstation for controlled molecule experiments. *Rev. Sci. Instrum.*, 96(2), February 2025.

[39] V. I. Gibalov and G. J. Pietsch. The development of dielectric barrier discharges in gas gaps and on surfaces. *J. Phys. D: Appl. Phys.*, 33(20):2618–2636, September 2000.

[40] A. Kramida and Y. Ralchenko. Nist atomic spectra database, nist standard reference database 78, 1999.

[41] S. S. Hodgman, R. G. Dall, L. J. Byron, K. G. H. Baldwin, S. J. Buckman, and A. G. Truscott. Metastable helium: A new determination of the longest atomic excited-state lifetime. *Phys. Rev. Let.*, 103(5):053002, July 2009.

[42] J. H. Gross. *Mass Spectrometry*. Springer International Publishing, 2017.

[43] K. Tanaka, H. Waki, Y. Ido, S. Akita, Y. Yoshida, T. Yoshida, and T. Matsuo. Protein and polymer analyses up to m/z 100 000 by laser ionization time-of-flight mass spectrometry. *Rapid Commun. Mass Spectrom.*, 2(8):151–153, August 1988.

[44] M. Karas, D. Bachmann, U. Bahr, and F. Hillenkamp. Matrix-assisted ultraviolet laser desorption of non-volatile compounds. *Int. J. Mass Spectrom.*, 78:53–68, September 1987.

[45] J. Schätti, M. Kriegleder, M. Debiossac, M. Kerschbaum, P. Geyer, M. Mayor, M. Arndt, and V. Köhler. Neutralization of insulin by photocleavage under high vacuum. *Chem. Commun.*, 55(83):12507–12510, 2019.

[46] J. B. Fenn. Electrospray wings for molecular elephants (nobel lecture). *Angew. Chem. Int. Ed.*, 42(33):3871–3894, August 2003.

[47] F. Sobott, H. Hernández, M. G. McCammon, M. A. Tito, and C. V. Robinson. A tandem mass spectrometer for improved transmission and analysis of large macromolecular assemblies. *Anal. Chem.*, 74(6):1402–1407, February 2002.

[48] M. S. Wilm and M. Mann. Electrospray and taylor-cone theory, dole's beam of macromolecules at last? *Int. J. Mass Spectrom.*, 136(2–3):167–180, September 1994.

[49] D. Duft, T. Achtzehn, R. Müller, B. A. Huber, and T. Leisner. Rayleigh jets from levitated microdroplets. *Nature*, 421(6919):128–128, January 2003.

[50] D. J. Douglas and J. B. French. Collisional focusing effects in radio frequency quadrupoles. *J. Am. Soc. Mass Spectrom.*, 3(4):398–408, May 1992.

[51] J. He, Q. Yu, L. Li, W. Hang, and B. Huang. Characteristics and comparison of different radiofrequency-only multipole cooling cells. *Rapid Commun. Mass Spectrom.*, 22(20):3327–3333, September 2008.

[52] M. Guilhaus, D. Selby, and V. Mlynski. Orthogonal acceleration time-of-flight mass spectrometry. *Mass Spectrom. Rev.*, 19(2):65–107, 2000.

[53] W. Paul. Electromagnetic traps for charged and neutral particles (nobel lecture). *Angew. Chem. Int. Ed.*, 29(7):739–748, July 1990.

[54] M. Born and E. Wolf. *Principles of optics*. Cambridge University Press, Cambridge, 7th anniversary edition edition, 2019.

[55] M. Arndt. De broglie's meter stick: Making measurements with matter waves. *Phys. Today*, 67(5):30–36, May 2014.

[56] C. Brand, S. Troyer, C. Knobloch, O. Cheshnovsky, and M. Arndt. Single-, double-, and triple-slit diffraction of molecular matter waves. *Am. J. Phys.*, 89(12):1132–1138, December 2021.

[57] O. Nairz, M. Arndt, and A. Zeilinger. Experimental verification of the heisenberg uncertainty principle for fullerene molecules. *Phys. Rev. A*, 65(3):032109, February 2002.

[58] A. D. Cronin, J. Schmiedmayer, and D. E. Pritchard. Optics and interferometry with atoms and molecules. *Rev. Mod. Phys.*, 81(3):1051–1129, July 2009.

[59] B. Brezger, L. Hackermüller, S. Uttenthaler, J. Petschinka, M. Arndt, and A. Zeilinger.

Matter-wave interferometer for large molecules. *Phys. Rev. Lett.*, 88(10):100404, February 2002.

[60] S. Nimmrichter, P. Haslinger, K. Hornberger, and M. Arndt. Concept of an ionizing time-domain matter-wave interferometer. *New J. Phys.*, 13(7):075002, July 2011.

[61] S. Nimmrichter and K. Hornberger. Theory of near-field matter-wave interference beyond the eikonal approximation. *Phys. Rev. A*, 78(2):023612, August 2008.

[62] C. Knobloch, B. A. Stickler, C. Brand, M. Sclafani, Y. Lilach, T. Juffmann, O. Cheshnovsky, K. Hornberger, and M. Arndt. On the role of the electric dipole moment in the diffraction of biomolecules at nanomechanical gratings. *Fortsch. Phys.*, 65(6–8), September 2016.

[63] K. Hornberger, S. Gerlich, H. Ulbricht, L. Hackermüller, S. Nimmrichter, I. V Gol'dt, O. Boltalina, and M. Arndt. Theory and experimental verification of kapitza–dirac–talbot–lau interferometry. *New J. Phys.*, 11(4):043032, April 2009.

[64] K. Simonović, R. Ferstl, A. Barlow, A. Shayeghi, C. Brand, and M. Arndt. Diffraction of polar molecules at nanomasks with low charge density. *Phys. Rev. Res.*, 6(3):033109, July 2024.

[65] R. E. Grisenti, W. Schöllkopf, J. P. Toennies, G. C. Hegerfeldt, and T. Köhler. Determination of atom-surface van der waals potentials from transmission-grating diffraction intensities. *Phys. Rev. Lett.*, 83(9):1755–1758, August 1999.

[66] P. Haslinger, N. Dörre, P. Geyer, J. Rodewald, S. Nimmrichter, and M. Arndt. A universal matter-wave interferometer with optical ionization gratings in the time domain. *Nat. Phys.*, 9(3):144–148, February 2013.

[67] S. Gerlich, L. Hackermüller, K. Hornberger, A. Stibor, H. Ulbricht, M. Gring, F. Goldfarb, T. Savas, M. Müri, M. Mayor, and M. Arndt. A kapitza–dirac–talbot–lau interferometer for highly polarizable molecules. *Nat. Phys.*, 3(10):711–715, August 2007.

[68] B. Brezger, M. Arndt, and A. Zeilinger. Concepts for near-field interferometers with large molecules. *J. Opt. B: Quantum Semiclass. Opt*, 5(2):S82–S89, April 2003.

[69] E.W. Schlag, J. Grotemeyer, and R.D. Levine. Do large molecules ionize? *Chem. Phys. Lett.*, 190(6):521–527, March 1992.

[70] E.W. Schlag and R.D. Levine. Ionization, charge separation, charge recombination, and electron transfer in large systems. *J. Phys. Chem.*, 96(26):10608–10616, 1992.

[71] C. H. Beckercor and K. J. Wufn. On the photoionization of large molecules. *J. Am. Soc. Mass Spectrom.*, 6(10):883–888, October 1995.

[72] Y. Hua, D. Häussinger, M. Mayor, V. Köhler, M. Strauss, M. F. X. Mauser, T. Kostersitz, P. Geyer, and M. Arndt. Neutralization of an oxytocin derivative by 355 nm photocleavage in high vacuum. *Helv. Chim. Acta*, 108(2), January 2025.

[73] Thomas Juffmann, Hendrik Ulbricht, and Markus Arndt. Experimental methods of molecular matter-wave optics. *Reports on Progress in Physics*, 76(8):086402, August 2013.

[74] B. Barwick, G. Gronniger, L. Yuan, S. Liou, and H. Batelaan. A measurement of electron-wall interactions using transmission diffraction from nanofabricated gratings. *J. Appl. Phys.*, 100(7), October 2006.

[75] M. Marksteiner, P. Haslinger, M. Sclafani, H. Ulbricht, and M. Arndt. Uv and vuv ionization of organic molecules, clusters, and complexes. *J. Phys. Chem. A*, 113(37):9952–9957, August 2009.

[76] Nicholas J. Turro. *Modern molecular photochemistry*. Univ. Science Books, Sausalito, Calif., 2. print. edition, 1991.

[77] Ulrich Kubitscheck, editor. *Fluorescence microscopy*. Wiley-VCH, Weinheim, second edition. edition, 2017. Includes bibliographical references and index. - Online resource; title from PDF title page (EBSCO, viewed April 5, 2017).

[78] R. Schinke. *Photodissociation Dynamics: Spectroscopy and Fragmentation of Small Polyatomic Molecules*. Cambridge University Press, April 1993.

[79] W. Vassen, C. Cohen-Tannoudji, M. Leduc, D. Boiron, C. I. Westbrook, A. Truscott, K. Baldwin, G. Birkl, P. Cancio, and M. Trippenbach. Cold and trapped metastable noble gases. *Rev. Mod. Phys.*, 84(1):175–210, February 2012.

[80] M. D. Morse, A. C. Puiu, and R. E. Smalley. Intramolecular vibrational relaxation: Effects on electronic nonradiative relaxation rates. *J. Chem. Phys.*, 78(6):3435–3444, March 1983.

[81] Joseph R. Lakowicz. *Principles of fluorescence spectroscopy*. Springer, New York, NY, third edition, corrected at 4. printing edition, 2010. Literaturangaben.

[82] R. Englman and J. Jortner. The energy gap law for radiationless transitions in large molecules. *Mol. Phys.*, 18(2):145–164, February 1970.

[83] M. Debiossac, J. Schätti, M. Kriegleder, P. Geyer, A. Shayeghi, M. Mayor, M. Arndt, and V. Köhler. Tailored photocleavable peptides: fragmentation and neutralization pathways in high vacuum. *Phys. Chem. Chem. Phys.*, 20(16):11412–11417, 2018.

[84] U. Sezer, P. Geyer, M. Kriegleder, M. Debiossac, A. Shayeghi, M. Arndt, L. Felix, and M. Mayor. Selective photodissociation of tailored molecular tags as a tool for quantum optics. *Beilstein J. Nanotechnol.*, 8:325–333, February 2017.

[85] S. J. Steinke, E. J. Piechota, L. M. Loftus, and C. Turro. Acetonitrile ligand photosubstitution in ru(ii) complexes directly from the 3mlct state. *J. Am. Chem. Soc.*, 144(44):20177–20182, October 2022.

[86] M. N. Dunbar, S. J. Steinke, E. J. Piechota, and C. Turro. Differences in photophysical properties and photochemistry of ru(ii)–terpyridine complexes of ch3cn and pyridine. *J. Phys. Chem. A*, 128(3):599–610, January 2024.

[87] C. Walther, St. Becker, G. Dietrich, H.-J. Kluge, M. Lindinger, K. Lützenkirchen, L. Schweikhard, and J. Ziegler. Photo fragmentation of metal clusters stored in a penning trap. *Z. Phys. D: At., Mol. Clusters*, 38(1):51–58, March 1996.

[88] J. Friedrich, S. Gilb, O. T. Ehrler, A. Behrendt, and M. M. Kappes. Electronic photodissociation spectroscopy of isolated irx62- (x=cl,br). *J. Chem. Phys.*, 117(6):2635–2644, August 2002.

[89] R.J. Beuhler and L. Friedman. Threshold studies of secondary electron emission induced by macro-ion impact on solid surfaces. *Nucl. Instr. Meth. Phys. Res.*, 170(1–3):309–315, March 1980.

[90] A. Brunelle, P. Chaurand, S. Della-Negra, Y. Le Beyec, and E. Parilis. Secondary electron emission yields from a csi surface under impacts of large molecules at low velocities. *Rap. Comm. Mass Spectr.*, 11(4):353–362, 1997.

[91] M. Tinkham. *Introduction to superconductivity*. International series in pure and applied physics. McGraw Hill, 2. ed edition, 1996.

[92] A. E. Lita, D. V. Reddy, V. B. Verma, R. P. Mirin, and S. W. Nam. Development of superconducting single-photon and photon-number resolving detectors for quantum applications. *J. Light. Technol.*, 40(23):7578–7597, December 2022.

[93] J. Bardeen, L. N. Cooper, and J. R. Schrieffer. Theory of superconductivity. *Phys. Rev.*, 108(5):1175–1204, December 1957.

[94] M. Guziewicz, A. Laszcz, J. Z. Domagala, K. Golaszewska, J. Ratajczak, R. Kruszka, M. Juchniewicz, A. Czerwinski, and W. Slysz. Structural analysis of epitaxial nbtin films. In Pawel Szczepanski, Ryszard Kisiel, and Ryszard S. Romaniuk, editors, *Electron Technology Conference 2013*, volume 8902, page 89022S. SPIE, July 2013.

[95] A. D. Semenov, G. N. Gol'tsman, and A. A. Korneev. Quantum detection by current carrying superconducting film. *Phys. C: Supercond.*, 351(4):349–356, April 2001.

[96] R. Cristiano, M. Ejrnaes, A. Casaburi, N. Zen, and M. Ohkubo. Superconducting nano-strip particle detectors. *Supercond. Sci. Technol.*, 28(12):124004, November 2015.

[97] J. J. Renema, R. Gaudio, Q. Wang, Z. Zhou, A. Gaggero, F. Mattioli, R. Leoni, D. Sahin, M. J. A. de Dood, A. Fiore, and M. P. van Exter. Experimental test of theories of the detection mechanism in a nanowire superconducting single photon detector. *Phys. Rev. Lett.*, 112(11):117604, March 2014.

[98] M. Hofherr, D. Rall, K. Ilin, M. Siegel, A. Semenov, H.-W. Hübers, and N. A. Gippius. Intrinsic detection efficiency of superconducting nanowire single-photon detectors with different thicknesses. *J. Appl. Phys.*, 108(1), July 2010.

[99] J. J. Renema, G. Frucci, Z. Zhou, F. Mattioli, A. Gaggero, R. Leoni, M. J. A. de Dood, A. Fiore, and M. P. van Exter. Universal response curve for nanowire superconducting single-photon detectors. *Phys. Rev. B*, 87(17):174526, May 2013.

[100] K. Suzuki, S. Shiki, M. Ukibe, M. Koike, S. Miki, Z. Wang, and M. Ohkubo. Hot-spot detection model in superconducting nano-stripline detector for kev ions. *Appl. Phys. Express*, 4(8):083101, July 2011.

[101] A. D. Semenov, P. Haas, H.-W. Hübers, K. Ilin, M. Siegel, A. Kirste, T. Schurig, and A. Engel. Vortex-based single-photon response in nanostructured superconducting detectors. *Phys. C: Supercond.*, 468(7–10):627–630, April 2008.

[102] M. Strauß, A. Shayeghi, M. F. X. Mauser, P. Geyer, T. Kostersitz, J. Salapa, O. Dobrovolskiy, S. Daly, J. Commandeur, Y. Hua, V. Köhler, M. Mayor, J. Benserhir, C. Bruschini, E. Charbon, M. Castaneda, M. Gevers, R. Gourgues, N. Kalhor, A. Fognini, and M. Arndt. Highly sensitive single-molecule detection of macromolecule ion beams. *Sci. Adv.*, 9(48), December 2023.

[103] D. H. Andrews, R. D. Fowler, and M. C. Williams. The effect of alpha-particles on a superconductor. *Phys. Rev.*, 76(1):154–155, July 1949.

[104] N. E. Booth, B. Cabrera, and E. Fiorini. Low-temperature particle detectors. *Annu. Rev. Nucl. Part. Sci.*, 46(1):471–532, December 1996.

[105] N. E. Booth and D. J. Goldie. Superconducting particle detectors. *Supercond. Sci. Technol.*, 9(7):493–516, July 1996.

[106] D. Twerenbold, J.-L. Vuilleumier, D. Gerber, A. Tadsen, B. van den Brandt, and P. M. Gillevet. Detection of single macromolecules using a cryogenic particle detector coupled to a biopolymer mass spectrometer. *Appl. Phys. Lett.*, 68(24):3503–3505, June 1996.

[107] M. Marksteiner, A. Divochiy, M. Sclafani, P. Haslinger, H. Ulbricht, A. Korneev, A. Semenov, G. Gol'tsman, and M. Arndt. A superconducting nbn detector for neutral nanoparticles. *Nanotechnology*, 20(45):455501, October 2009.

[108] J. Ladislas Wiza. Microchannel plate detectors. *Nucl. Instrum. Meth.*, 162(1–3):587–601, June 1979.

[109] R. Rispoli, E. De Angelis, L. Colasanti, N. Vertolli, S. Orsini, J. A. Scheer, A. Mura, A. Milillo, P. Wurz, S. Selci, A. M. Di Lellis, R. Leoni, M. D'Alessandro, F. Mattioli, and S. Cibella. Elena microchannel plate detector: absolute detection efficiency for low energy neutral atoms. *Opt. Eng.*, 52(5):051206, May 2013.

[110] K. Fehre, D. Trojanowskaja, J. Gatzke, M. Kunitski, F. Trinter, S. Zeller, L. Ph. H. Schmidt, J. Stohner, R. Berger, A. Czasch, O. Jagutzki, T. Jahnke, R. Dörner, and M. S. Schöffler. Absolute ion detection efficiencies of microchannel plates and funnel microchannel plates for multi-coincidence detection. *Rev. Sci. Instrum.*, 89(4), April 2018.

[111] O. Carnal, A. Faulstich, and J. Mlynek. Diffraction of metastable helium atoms by a transmission grating. *Appl. Phys. B*, 53(2):88–91, August 1991.

[112] O. F. Hagena. Cluster ion sources (invited). *Rev. Sci. Instrum.*, 63(4):2374–2379, April 1992.

[113] O. F. Hagena. Condensation in free jets: Comparison of rare gases and metals. *Z. Phys. D: At., Mol. Clusters*, 4(3):291–299, September 1987.

[114] H. Khemliche, P. Rousseau, P. Roncin, V. H. Etgens, and F. Finocchi. Grazing incidence fast atom diffraction: An innovative approach to surface structure analysis. *Appl. Phys. Lett.*, 95(15), October 2009.

[115] C. Brand, M. Debiossac, T. Susi, F. Aguillon, J. Kotakoski, P. Roncin, and M. Arndt. Coherent diffraction of hydrogen through the 246 pm lattice of graphene. *New J. Phys.*, 21(3):033004, March 2019.

[116] P. Rousseau, H. Khemliche, A. G. Borisov, and P. Roncin. Quantum scattering of fast atoms and molecules on surfaces. *Phys. Rev. Lett.*, 98(1):016104, January 2007.

[117] P. Rousseau, H. Khemliche, N. Bundaleski, P. Soulisse, A. Momeni, and P. Roncin. Surface analysis with grazing incidence fast atom diffraction (gifad). *J. Phys. Conf. Ser.*, 133:012013, October 2008.

A. Diffraction pattern model

This appendix provides the detailed derivation of the model used to fit the experimental diffraction patterns described in the main text.

As established in chapter 3, the far-field diffraction pattern of a grating is described by $I_0(\lambda, x)$:

$$I_0(\lambda, x) \propto \left(\frac{\sin \frac{\alpha(x)}{\lambda}}{\frac{\alpha(x)}{\lambda}} \right)^2 \left(\frac{\sin \frac{N\beta(x)}{\lambda}}{\sin \frac{\beta(x)}{\lambda}} \right)^2 , \tag{A.1}$$

with $\alpha(x) = a\pi \sin \vartheta_{\text{slit}}$ and $\beta(x) = d\pi \sin \vartheta_{\text{grat}}$.

For the fit of metastable helium diffraction, deviations from the ideal Kirchhoff approximation must be incorporated. The most relevant corrections arise from incoherence of the source and from atom-surface interactions at the nanomask. The latter reduce transmission close to the slit edges. Rather than modeling the van der Waals/Casimir–Polder potential explicitly, these effects are accounted for phenomenologically by introducing an effective slit width $s_{\text{eff}} \leq s$ [65]. Additionally, the model accounts for the finite velocity spread and for residual decoherence arising from collimation.

Velocity spread

Even under perfectly coherent conditions, the finite velocity spread of the atoms due to the source broadens the diffraction peaks. This is expressed as a distribution of de Broglie wavelengths with full width at half maximum $\Delta\lambda_{\text{He}^*} = 2\sqrt{2 \ln 2}\, \sigma_{\lambda_{\text{He}^*}}$. Assuming a Gaussian profile, each atom is treated as a Gaussian wavepacket $w(\lambda)$ in wavelength space:

$$w(\lambda) = \frac{1}{\sqrt{2\pi}\sigma_{\lambda_{\text{He}^*}}} \exp\left(-\frac{(\lambda - \lambda_{\text{He}^*})^2}{2\sigma^2_{\lambda_{\text{He}^*}}} \right) , \tag{A.2}$$

with normalization $\int w(\lambda)\, \mathrm{d}\lambda = 1$. The raw diffraction pattern including velocity spread is then given by

$$I_{\text{raw}}(x) = \int I_0(\lambda, x)\, w(\lambda)\, \mathrm{d}\lambda \, . \tag{A.3}$$

Decoherence from collimation

Residual decoherence due to finite collimation is modeled phenomenologically by a Gaussian convolution [74]. A Gaussian kernel is chosen because angular deviations of the beam are

approximately normally distributed, and the resulting convolution captures the observed reduction in fringe contrast:

$$g(x) = \frac{1}{\sqrt{2\pi}\sigma_{\text{coll}}} \exp\left(-\frac{x^2}{2\sigma_{\text{coll}}^2}\right) , \tag{A.4}$$

normalized such that $\int g(x)\,\mathrm{d}x = 1$. The observed intensity distribution is therefore:

$$I_{\text{obs}}(x) = (I_{\text{raw}} * g)(x) = \int I_{\text{raw}}(\xi)\, g(x-\xi)\,\mathrm{d}\xi \, . \tag{A.5}$$

This integral expression defines the model function used to fit the experimental diffraction pattern.